scientific reports

Check for updates

OPEN

Experimental and computational approach on the corrosion inhibition properties of two newly pyrazole derivatives on carbon steel in acid medium

Nawal Setti[1], Asma Barrahi[2], Mohamed Maatallah[3], Yassine Kaddouri[1], Taibi Ben Hadda[4], Halima Outada[5], Abhinay Thakur[6], Rachid Touzani[1], Khalid Karrouchi[7], Hatem A. Abuelizz[8], Burak Dikici[9], Abdelkader Zarrouk[2]✉ & Ali Dafali[1]✉

In the current investigation, the efficiency inhibition of two newly synthesized bi-pyrazole derivatives, namely 2,3-bis[(bis((1 H-pyrazol-1-yl) methyl) amino)] pyridine (*Tetra-Pz-Ortho*) and 1,4-bis[(bis((1 H-pyrazol-1-yl) methyl) amino)] benzene (*Tetra-Pz-Para*) for corrosion of carbon steel (C&S) in 1 M HCl medium was evaluated. A Comparative study of inhibitor effect of *Tetra-Pz-Ortho* and *Tetra-Pz-Para* was conducted first using weight loss method and EIS (Electrochemical Impedance Spectroscopy) and PDP (Potentiodynamic Polarisation) techniques. *Tetra-Pz-Ortho* and *Tetra-Pz-Para* had a maximum inhibition efficacy of 97.2% and 96.2% respectively at optimum concentration 10^{-3}mol/L and temperature 303 K, according to the data, suggesting that they are both effective inhibitors. The inhibition effectiveness of *Tetra-Pz-Ortho* and *Tetra-Pz-Para* increases significantly with higher concentration but decreases as temperature rises. The adsorption study demonstrated that the two molecules tested follow the Langmuir adsorption isotherm and chemically adsorbed on the metallic surface. The polarization methods showed that both compounds *Tetra-Pz-Ortho* and *Tetra-Pz-Para* were classified as mixed inhibitors. Based on the electrochemical impedance technique, the addition of the two inhibitors increased the charge transfer resistance and decreased the double layer capacity. In addition, the scanning electron microscopy (SEM) showed that the surface roughness of the C&S was considerably reduced in the presence of both *Tetra-Pz-Ortho* and *Tetra-Pz-Para* compared to its roughness without the inhibitors, indicated that the two inhibitors are effectively absorbed onto the carbon steel surface. These results were supported by elemental analysis of the metal/solution interface using X-ray photoelectron spectroscopy (XPS), for the two molecules tested. All studies demonstrated that the compound *Tetra-Pz-Ortho* is the most effective inhibitor. The DFT calculations and Monte Carlo/Molecular dynamic (MC/MD) simulations were treated and discussed for both compounds *Tetra-Pz-Ortho* and *Tetra-Pz-Para* in order to explain their interfacial approach and compared them to experimental results. The computational results of quantum chemistry were in agreement with those acquired by experimental methods.

Keywords Pyrazole derivatives, Carbon steel, Electrochemical techniques, Surface characterisation techniques, Theoretical methods

[1]LCEA Laboratory, Faculty of Sciences, Mohammed Premier University, Oujda, Morocco. [2]Laboratory of Materials, Nanotechnology and Environment, Faculty of Sciences, Mohammed V University in Rabat, P.O. Box. 1014, Rabat, Morocco. [3]Laboratory of Molecular Chemistry, Faculty of Sciences Semlalia, Cadi Ayyad University, PO Box 2390, Marrakech, Morocco. [4]Euromed Research Center, Euromed Faculty of Pharmacy, Euromed University of Fes (UEMF), Meknes Road, Fez 30000, Morocco. [5]National School of Commerce and Management, Mohammed Premier University, Oujda 60046, Morocco. [6]Division of Research and Development, Lovely Professional University, Phagwara, Punjab, India. [7]Laboratory of Analytical Chemistry and Bromatology, Team of Formulation and Quality Control of Health Products, Faculty of Medicine and Pharmacy, Mohammed V University in Rabat, Rabat, Morocco. [8]Department of Pharmaceutical Chemistry, College of Pharmacy, King Saud University, PO Box 2457, Riyadh

11451, Saudi Arabia. [9]Department of Mechanical Engineering, Ataturk University, Erzurum 25240, Turkey. ✉email: azarrouk@gmail.com; dafali2@gmail.com

Degradation of metals like steel, which is a global industrial activity, is often viewed as a threat to systems striving for greater sustainability. Steel is used in a several industrial processes in acid solutions (HCl, H_2SO_4, HNO_3 or H_3PO_4) for cleaning, descaling or pickling operations so as to remove undesirable scale and rust[1–5]. Carbon steel is one of the metals with weak behavior towards acidic environments, giving rise to corrosion attack and consequently a horrible cost in industrial field[6,7]. Corrosion inhibitors are classed based on their chemical structure, methods of action, and other properties[8,9]. One of the most important types is organic corrosion inhibitors, having gained the highest importance due to their simplicity of synthesis, low cost, and strong protective ability[10]. Corrosion organic inhibitors played an important role to reduce corrosion damages and consequently hinder the degradation of the metal[11–13]. Based on the available data, organic inhibitors function via adsorption and protect the metal through film formation[14]. The great majority of the corrosion organic inhibitors are heterocyclic compounds containing heteroatoms (O-atoms, N-atoms and S-atoms) as well as the aromatic rings rich in lone pair of electrons and π-electrons delocalised which are transferred to iron surface having vacant d-orbital, giving thus, high efficiency[15–20]. Furthermore, compounds with Sulphur atoms efficiently block sulphuric acid, whereas organic anticorrosion substances containing nitrogen are beneficial for metals in corrosive HCl acid. Similarly, molecules that include Sulphur and nitrogen function well to prevent corrosion in both media[21]. The adsorption ability of organic inhibitors is strongly related to their planar structure, the nature of functional groups, aromatic rings, steric as well as electronic factors[22,23]. Moreover, molecules types with wide geometric structure with the presence of heteroatoms and aromatic rings are proven to be good corrosion inhibitors[24]. It was demonstrated that these physicochemical characteristics, which are connected to the electron-donator action of the electron-rich groups, are the primary determinants of a good adsorption of these inhibitors on metal surfaces[25]. On the other hand, heterocyclic molecules have an interesting attention as bioactive molecules in pharmaceutical industry; We can quote for example fragments of molecules such as Thiazoles, Pyrimidines, Benzotriazole and Pyrazoles derivatives[26–28].

The present study aims to investigate the protective impact of two synthesized bis-pyrazole derivatives ***Tetra-Pz-Ortho*** and ***Tetra-Pz-Para*** (Fig. 1), on C&S corrosion employing a gravimetric and electrochemical techniques in a 1 M hydrochloric acid solution. These compounds are easy to synthesise and are considered to be heterocyclic compounds of therapeutic interest[28]. Among the methods employed, the weight loss measurement was chosen to assess the thermodynamic activation parameters and the adsorption isotherm. EIS and PDP techniques were used to examine corrosion process and to determine electrochemical parameters of C&S both before and after the two inhibitors (***Tetra-Pz-Ortho*** & ***Tetra-Pz-Para***) were added in acid solution. Surface analysis using SEM was performed for C&S specimens with the aim to determine the chemical composition of the inhibitor film and follow of its adsorption mode. The correlation between the structures of molecules ***Tetra-Pz-Ortho*** & ***Tetra-Pz-Para*** and their inhibitory properties have been investigated by utilizing computational chemistry methods. In order to do this approach clearly, and to better interpret the mechanism of inhibition, the reactivity descriptors of the two molecules have been calculated using density functional theory (DFT) method. The mechanism of the C&S-inhibitor interaction has been investigated using MD simulations.

Experimental section

Organic synthesis and chemical data

The two tetra N-alkylated heterocyclic compounds: 2,3-bis[(bis((1H-pyrazol-1-yl) methyl) amino)] pyridine (***Tetra-Pz-Ortho***) and 1,4-bis[(bis((1H-pyrazol-1-yl) methyl) amino)] benzene (***Tetra-Pz-Para***) were prepared from the benzene-1,4-diamine and 2,3-diaminopyridine using the synthesis procedures described in the Scheme 1. The first step consists of the preparation of 1-(hydroxymethyl)-3,5-dimethylpyrazole from (Z)-

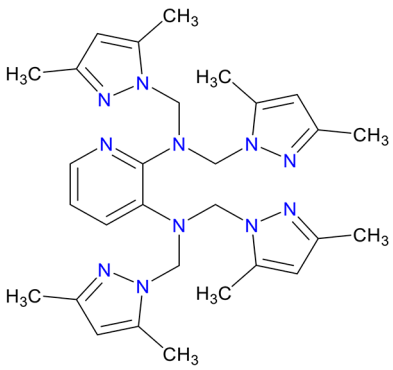

*2,3-bis[(bis((1H-pyrazol-1-yl) methyl) amino)] pyridine (**Tetra-Pz-Ortho**)*

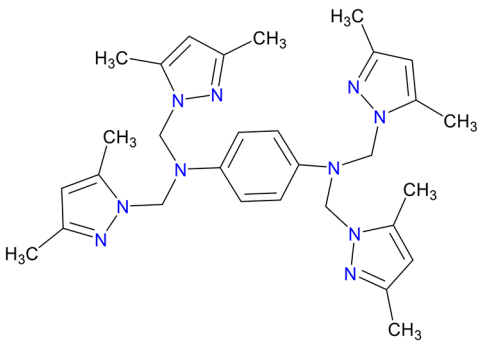

*1,4-bis[(bis((1H-pyrazol-1-yl) methyl) amino)] benzene (**Tetra-Pz-Para**)*

Fig. 1. Molecular Structures of ***Tetra-Pz-Ortho*** and ***Tetra-Pz-Para***.

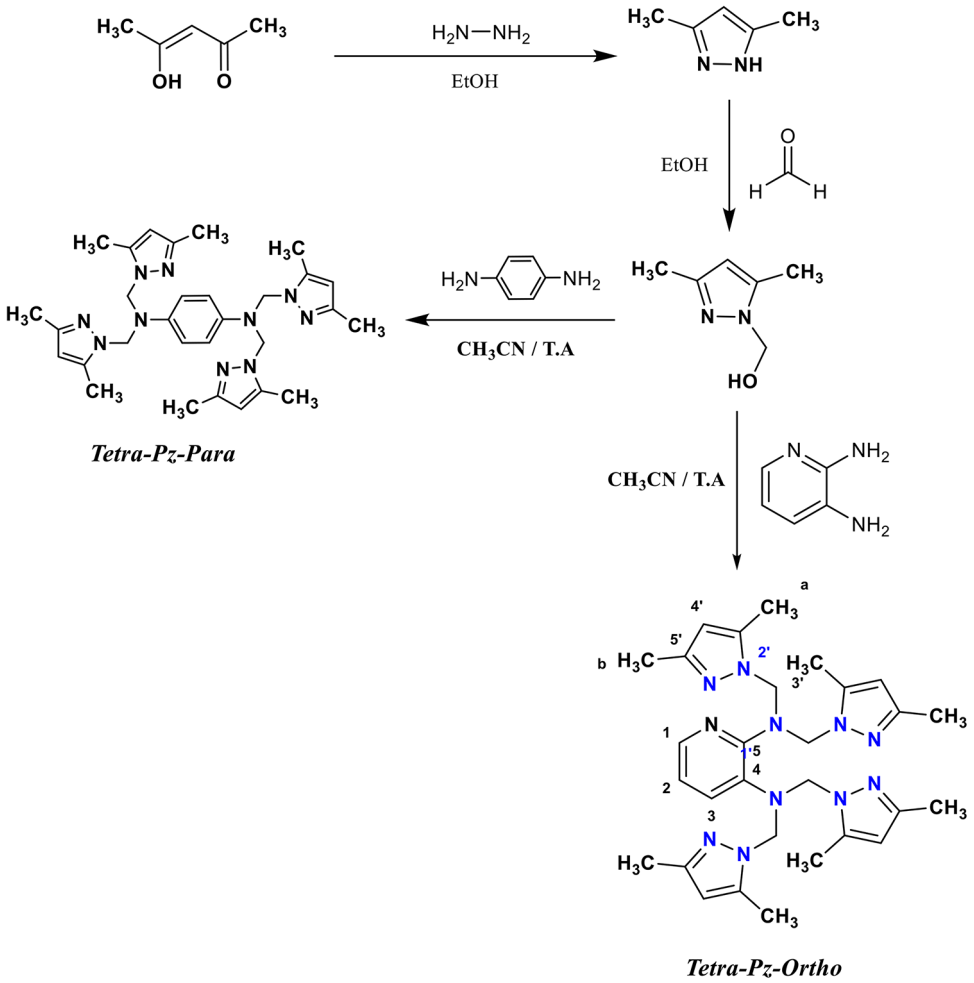

Scheme 1. Synthesis of ***Tetra-Pz-Ortho*** and ***Tetra-Pz-Para***.

4-hydroxypent-3-en-2-one. It is an important common step for the preparation of both molecules. The new synthesized compound *2,3-bis[(bis((1H-pyrazol-1-yl) methyl) amino)] pyridine* ($C_{29}H_{39}N_{11}$ with MW: 541.71, other nomenclature: *N*, *N*, *N'*, *N'-tetra-((3,5-dimethyl-1 H-pyrazol-1-yl) methyl) pyridine-2,3-diamine)* was prepared from the condensation of 1-(hydroxymethyl)-3,5-dimethylpyrazole with pyridine-2,3-diamine under optimum gentle conditions and was characterized using FTIR and NMR (1 H & 13 C) spectroscopy as follows[29]:

FTIR (KBr, cm^{-1}): 3000(=C-H); 2363 (C-H); 1555 (C=C); 1532 (C-C); 1396 (C-N); 1304 (C=N); 1132 (N-N); 782 (=C-H).

NMR ^{1}H (CD_2Cl_2, 500 MHz) δ ppm : 7.13 (d, 1H, CH (1)); 6.57 (d, 1H, CH (3)); 6.06 (dd, 1H, CH (2)); 5.89 and 5.80 (s, 4H, CH (4')); 5.51 and 5.42 (s, 8 H, CH_2); 2.45 (s, 12 H, CH_3 (a, b)).

NMR^{13}C (CD_2Cl_2, 500 MHz) δ ppm: 140.09 (C (1)); 138.68 (C (4, 5')); 148.42 and 138.99 (C (3')); 109.53 (C (2)); 107.94 (C (3)); 105.89, 105.13 and 105.05 (C (4')); 56.48 (C (CH_2)); 13.14, 10.82 and 10.37 (C (CH_3)).

Yield 73.91%, **Mp** = 116–118 °C.

The molecule1,4-bis[(bis((1H-pyrazol-1-yl) methyl) amino)] benzene (or *N*, *N*, *N'*, *N'- tetra -[(3,5 -dimethyl-1-pyrazolyl) methyl]-para-phenylenediamine*) has been resynthesized following the same procedures as those for the preparation of (***Tetra-Pz-Ortho***), as described in a previous work[30,31].

Electrolyte and materials

The blank electrolyte utilized in this study is a commercial hydrochloric acid solution 37%, which has been diluted to 1 M. In the purpose of preparing the various concentrations of the inhibitor, the appropriate quantities were weighed using an electronic balance, placed in a graduated flask, and then completed with the blank solution, followed by thorough mixing to achieve homogeneity. Consequently, solutions with concentrations ranging from 10^{-3} M to 10^{-6} M were prepared for weight loss and electrochemical analyses. The C&S metal

plates tested in this study possess the following chemical composition: 0.370% (C), 0.230% (Si), 0.680% (Mn), 0.016% (S), 0.077% (Cr), 0.011% (Ti), 0.059% (Ni), 0.009% (Co), 0.160% (Cu), with the remainder being iron. The C&S samples are disc-shaped with an area of 1 cm^2 for electrochemical testing, and square pieces measuring 2.5 cm × 2.5 cm × 0.05 cm for gravimetric measurements. These samples were prepared and cleaning according to ASTM G1-03 standard procedures[32], the specimens were polished using a range of emery paper from grit 180 to 1200, followed by rinsing with bidistilled water and acetone, drying, then immersion in the 1 M hydrochloric acid solution, both with and without the addition of various doses of inhibitors for both experimental methods. The immersion time employed for the concentration effect test was 6 h at 303 K for the weight loss method, while for the temperature effect study 303 to 333 K, the immersion time was 1 h. Each experiment was carried out in triplicate, with three carbon steel sheets weighed, and the resulting averages were calculated.

Electrochemical measurements

Concerning electrochemical study, we used a three-electrode cell; WE (Working Electrode) with a surface of C&S that has been prepared before, RE (reference electrode) in which based on SCE (Saturated Calomel Electrode) and CE (counter electrode) that is in platinum. This cell, with double-wall thermostated and a capacity of 100mL, is connected to a potentiostat/galvanostat PGZ-100 controlled by a "Voltamaster4" software computer, which provides the Tafel curves and impedance diagrams. For the different concentrations of inhibitors, a stabilisation step of the working electrode, maintained at the solution for 30 min, is necessary in order to establish a steady-state open circuit potential (OCP). the polarization curves plots carried out in a range of potential from − 800 to -100 mV by respecting a scan rate of 0.5 mV/sec. EIS diagrams were made in an interval of frequency from 100 kHz to 10 mHz with AC signal of amplitude 10 mV at OCP potential.

Surface analysis technical

The surface of C&S specimen has been explored by the device SEM (Scanning Electron Microscopy) model TESCAN VEGA3-EDAX. Images from scanning electron microscopy (SEM) were taken with an accelerating voltage of 10 kV and a magnification of 1.00 kx. Sample preparation on the C&S substrate follows the same procedure as described in Sect. 2.3. The obtained SEM micrographs of the tested specimens' surface of C&S were observed and analysed before and after immersion in 1 M HCl solution for 24 h without and with ***Tetra-Pz-Ortho*** and ***Tetra-Pz-Para***, to assess the type and structure of the shielding layer that has been deposited.

X-ray photoelectron spectroscopy (XPS SPECS-Flex) was used to generate XPS spectra. The source was a monochromatic Al-Kα X-ray source (hv = 1486.71 eV) with an approximate 3 mm X-ray beam. The analyzer and its average surface analysis lens were operating with a pass energy of 40 eV. A charge correction was implemented during the analytical phase to counteract charge effects, with the binding energy (BE) of C 1s (285.0 eV) acting as the internal reference. A non-linear least-squares method utilizing a Shirley baseline and a Gaussian-Lorentzian combination was used to deconvolve the XPS spectra. This deconvolution was mostly carried out on all spectra using Casa-XPS software. These XPS studies were carried out with and without inhibitors on the steel surface. C&S samples were prepared in compliance with the gravimetric technique test protocol, dried, and inspected thereafter.

UV-visible analysis

Ultraviolet-visible absorption spectrophotometry (UV-Visible) has been also used to investigate the behaviour's mechanism of ***Tetra-Pz-Ortho*** and ***Tetra-Pz-Para*** with C&S-substrate surfaces in 1 M HCl environment. the solutions were prepared in the presence of inhibitors ***Tetra-Pz-Ortho*** and ***Tetra-Pz-Para*** and analysed by UV-visible spectrometer, before and after immersion of C&S samples. The samples are completely immersed there in and left for 24 h in the tested inhibitory solution at the working temperature. 200–800 nm was the wavelength range that was investigated, and a Jenway 67 series UV–visible spectrophotometer was employed.

Quantum computing method DFT

Quantum computing

The electronic properties of of ***Tetra-Pz-Ortho*** and ***Tetra-Pz-Para*** were studied using the quantum chemical method to foretell a possible reactivity tendency of these compounds. In order to achieve this, a DFT calculation is used to determine the quantum chemical descriptors using B3LYP functional and 6-31G(d, p) basis set, treated by the Gaussian (09 W) 2013 program module[33]. The calculation of the quantum-chemical descriptors was made according to equations described in previous work[23,34].

Monte Carlo and molecular simulations study details

The Monte Carlo (MC) and molecular dynamics (MD) simulations methods were adopted to examine the low configuration adsorption energy and the adsorption mode of the interactions of molecules ***Tetra-Pz-Ortho*** and ***Tetra-Pz-Para*** on the metal area. The Adsorption Locator module in the Materials Studio 7.0 package was used to perform the Monte Carlo simulation[35]. The simulation was carried out with iron crystal with imported and cleaved along (110) plane (Fe (110)) with a slab of 5 Å to prevent any arbitrary impacts at the boundaries. In an effort to provide the two inhibitors a broad surface area for interaction, the Fe (110) plane was extended to a (10 × 10) super cell, and a 20 Å vacuum was created along the z-axis. We added 200 molecules of water to the simulation box to replicate the real corrosion environment. MD simulation was performed to evaluated the different low energy configurations of the interaction between ***Tetra-Pz-Ortho*** and ***Tetra-Pz-Para*** inhibitor molecules and the Fe surface in 200 water molecules and one 5HCl ($5H_3O^+$, $5Cl^-$). The calculations were carried out in a simulation box 24.82Å×24.82Å×38.11Å with periodic boundary conditions. The Condensed phase Optimized Molecular Potentials for Atomistic Simulation Studies (COMPASS)[36,37] force field was used with a time step of 1 fs and a simulation time of 500 ps. The simulation temperature was set at 303 K under NVT

(constant volume and temperature) ensemble and controlled by an Andersen thermostat. In simulation system, the interaction and binding energies are determined using the equations below:

$$E_{Interaction} = E_{Total} - (E_{Surface} + E_{Inhibitor}) \text{ and } E_{Binding} = -E_{Interaction} \quad (1)$$

where E_{total} is the total energy of the metal surface and adsorbed inhibitor molecule, $E_{surface}$ is the energy of the surface, and $E_{inhibitor}$ is the energy of the inhibitor.

Results and interpretation

EIS analysis

The EIS (Electrochemical Impedance Spectroscopy) is relevant electrochemical non-destructive techniques widely used in corrosion domain; it allows the corrosion inhibition potential to be assessed by exploring the interactions in the vicinity of the acid solution /metal interface. The mechanism of the electrochemical process and the phenomena of corrosion are closely related. The major focus of corrosion research is on the features of corrosion that take place at the interface between the electrolyte and the metal surface[38]. Therefore, the system studied C&S/solution of ***Tetra-Pz-Ortho*** and ***Tetra-Pz-Para*** was handled using the EIS technique, which permits the charting of the Nyquist and Bode diagrams, following stabilization by immersion in solutions for 30 min. Among the parameter reflecting the anti-corrosion efficacy for this technical, a simple method to measure efficiency is to identify the polarisation resistance, which is often estimated as the region encircled by the semicircle in Nyquist plots (η_Z(%)) according the following equation

$$\eta_Z\,(\%) = \left(\frac{R_{p,Inh} - R_{p,free}}{R_{p,Inh}}\right) \times 100 \quad (2)$$

The polarization resistance in inhibited and uninhibited solutions is denoted by R_{Pinh} and R_{Pfree}, respectively.

Figure 2 displays the Nyquist and Bode-phase graphs of C&S in the inhibited and uninhibited systems. The Nyquist plots show depressed capacitive semicircles, as can be shown, indicating that a charge transfer mechanism governs the ***Tetra-Pz-Para***& ***Tetra-Pz-Ortho*** and C&S /1 M HCl systems. It can be seen that all the Nyquist plots (Fig. 2a) show similar capacitive semicircles, indicating that the inhibition and uninhibited systems use the same reaction mechanism. Additionally, a rise in inhibitor amounts is linked to an increase in capacitive semicircle size; this phenomenon may be explained by an increase in ***Tetra-Pz-Ortho*** and ***Tetra-Pz-Para*** adsorbed molecules' surface coverage on the C&S surface[39]. A single peak is shown in bode-phase plots (Fig. 2b) for both cases tested, revealing one time constant. The maximum phase angle (in absolute value) and the frequency interval of gets bigger by adding of ***Tetra-Pz-Ortho*** and ***Tetra-Pz-Para***, showing a good adsorption of these inhibitory molecules on C&S interface[40]. To utilize the electrochemical impedance spectroscopy (EIS) data, an electrical circuit model was applied to fit the EIS spectra. This model consisted of the electrolyte resistance (R_s), the polarization resistance (R_p, which is equal to the sum of R_{ct} and R_f[41]), and the constant phase element (CPE), as shown in Fig. 3. The double-layer capacitance (Cdl) was replaced with the CPE impedance in order to improve the EIS results from the experiment. Equations 3 and 4 provide definitions for this substitution[42]:

$$Z_{CPE} = A^{-1}(i\omega)^{-1} \quad (3)$$

$$C_{dl} = \left(A \times R_p^{1-n}\right)^{1/n} \quad (4)$$

where *n*, *A*, *i*, and *w* symbolize the deviation index, the *CPE* constant, the imaginary number, and the angular frequency, respectively.

The basic parameters presented in Table 1 were established using the EIS diagram fitting findings for ***Tetra-Pz-Ortho*** and ***Tetra-Pz-Para*** at different doses. The values of R_p attained maximum loop diameter of 705.7 and 562.8 Ω cm^2 at 10^{-3} M for ***Tetra-Pz-Ortho*** and ***Tetra-Pz-Para***, respectively. Table 1 also demonstrates an increase in efficiency with concentration of inhibitors and the η_Z(%) values reached **96.9%** and **96.2%** at 10^{-3} M concentration for ***Tetra-Pz-Ortho*** and ***Tetra-Pz-Para***, respectively. These results show that ***Tetra-Pz-Ortho*** and ***Tetra-Pz-Para*** have extremely good inhibitory properties. The augmentation in values of R_p and the concurrent decline in C_{dl} as function of raising concentration of inhibitors, so that the R_s values rise after adding ***Tetra-Pz-Ortho*** and ***Tetra-Pz-Para*** molecules, reveal the substitution of H_2O molecules and chlorine ions at the C&S surface by ***Tetra-Pz-Ortho*** and ***Tetra-Pz-Para*** molecules, implying the rise in the thickness of the electrical double layer, and diminishing the local dielectric constant, which indicated that ***Tetra-Pz-Ortho*** and ***Tetra-Pz-Para*** act as the good inhibitors at the interface C&S/solution[43].

A comparative study of diagrams of phase angle and impedance module |Z| for C&S in presence of ***Tetra-Pz-Ortho*** and ***Tetra-Pz-Para*** at 10^{-3} M in 1 M HCl show a slight difference between the loop diameters of the two inhibitors, giving closely efficiencies (96.9% and 96.2%), respectively. All that justifies the excellent inhibitor effect whether for ***Tetra-Pz-Ortho*** or ***Tetra-Pz-Para***, with a slight distinction for ***Tetra-Pz-Ortho***, by covering a large area of metal, which lead to the efficient protection. This high rise of η_Z(%) is certainly due to the presence of four pyrazole rings in each molecule and their position in the aromatic ring (benzene and pyridine). Indeed, there are a lot of heteroatoms in these compounds, more than ten N-atoms + amino form, in addition to their molecular size larger, building a chelate form in ***Tetra-Pz-Ortho*** and leading to a covering of C&S-surface. This chelates effect may lead to the greater affinity of chelating ligands (pyrazole) for the iron ion, giving a significant inhibitor effect and this is the source of these molecules' highly active centres, which increase adsorption on the C&S surface these molecules' highly active centres, which increase adsorption on the C&S surface. Furthermore,

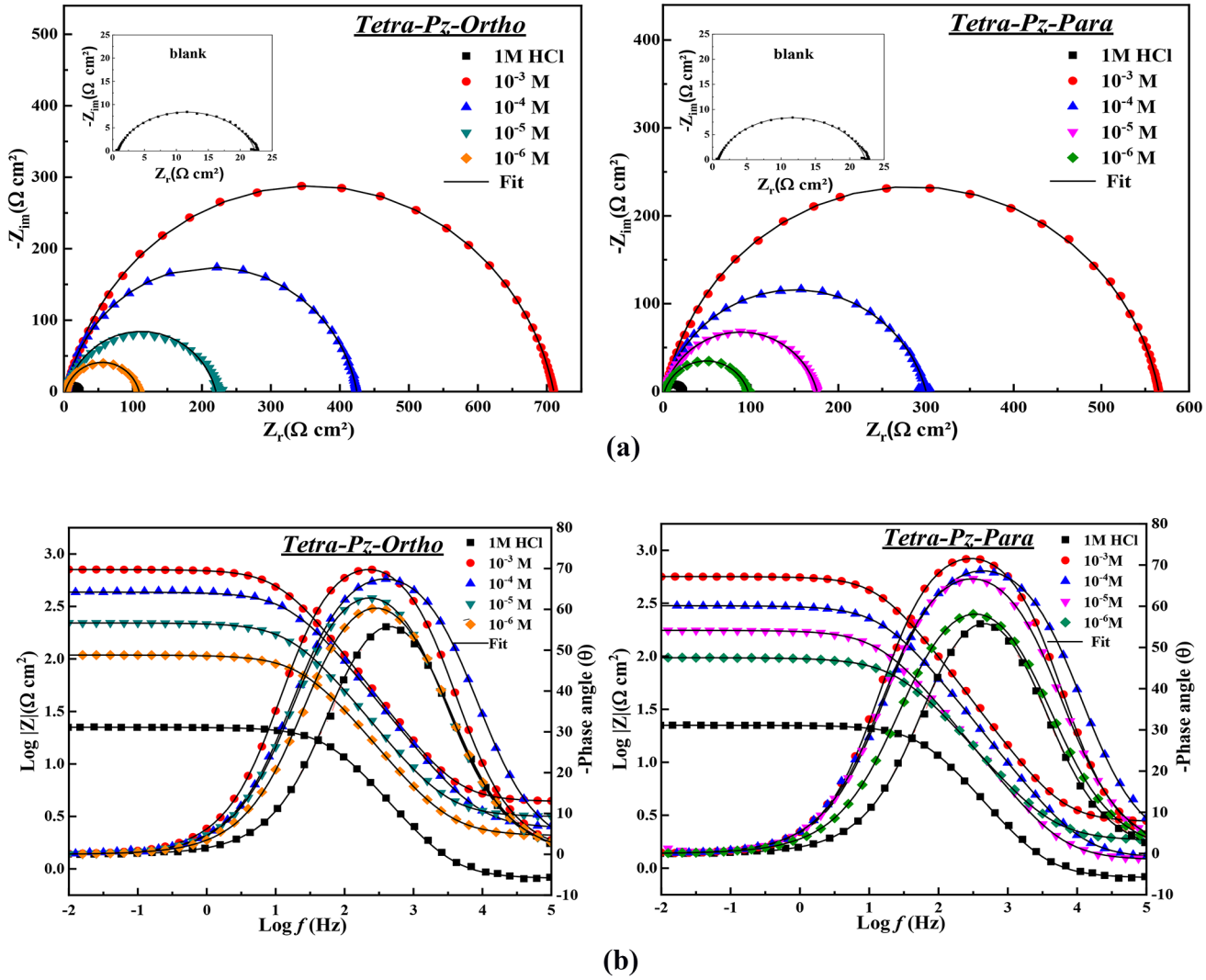

Fig. 2. (**a**) Nyquist diagrams for C&S /1 M HCl/***Tetra-Pz-Ortho*** and ***Tetra-Pz-Para*** systems. (**b**) Bode-phase diagrams for C&S/1 M HCl/***Tetra-Pz-Ortho*** and ***Tetra-Pz-Para*** systems.

Fig. 3. Equivalent circuit to simulate impedance spectra of system C&S / inhibitors.

Tetra-Pz-Ortho and ***Tetra-Pz*** have larger values of η_Z(%), which can be attributed to their broad molecular structures and the number of nitrogen lone pairs that create a denticity, particularly in ***Tetra-Pz-Ortho.*** A same comparative analysis of parameters impedance module |Z| and phase angle represented in Fig. 2b was carried out and illustrated this excellent inhibitory effect of ***Tetra-Pz-Ortho*** compared to ***Tetra-Pz-Para***, at the optimal concentration.

The double layer capacity C_{dl} shows also a decrease as function of concentration of inhibitors, and fitted in parameter A that decreases from 132.1 10^{-6} Ω^{-1} s^n cm^{-2} at 10^{-6} M to 32.7 10^{-6} Ω^{-1} s^n cm^{-2} at 10^{-3} M and from 143.5 10^{-6} Ω^{-1} s^n cm^{-2} at 10^{-6} M to 33.5 10^{-6} Ω^{-1} s^n cm^{-2} at 10^{-3} M for ***Tetra-Pz-Ortho*** and ***Tetra-Pz-Para***, respectively. Furthermore, the A values of the system without inhibitors are higher than those of the protected system, this uncovers that the investigated ***Tetra-Pz-Ortho*** and ***Tetra-Pz-Para*** interact with the C&S surface and thus, blocking the uncovered active sites of the metal. Also, the increase in ***n*** values upon the addition of both ***Tetra-Pz-Ortho*** and ***Tetra-Pz-Para*** results from a decrease in the heterogeneity of the C&S surface[28]. This indicates that the process of interfacial remains unchanged and that a protecting film of inhibitors can be

	Conc. (M)	R_s (Ω cm^2)	R_p (Ω cm^2)	10^6×A ($\Omega^{-1}s^n cm^{-2}$)	n	C_{dl} (μF cm^{-2})	χ^2	τ (ms)	η_z(%)
HCl	Blank	0.8	21.57	293.9	0.85	116.2	0.002	2.51	***
Tetra-Pz-Ortho	10^{-3}	4.2	705.7	32.7	0.87	18.6	0.005	13.13	**96.9**
	10^{-4}	2.6	430.9	44.5	0.86	23.4	0.009	10.08	95.0
	10^{-5}	3.1	217.2	84.8	0.84	39.3	0.004	8.54	90.1
	10^{-6}	2.1	106.9	132.1	0.83	55.2	0.002	5.90	79.8
Tetra-Pz-Para	10^{-3}	2.8	562.8	33.5	0.88	19.5	0.004	10.97	**96.2**
	10^{-4}	1.8	298.8	67.2	0.84	31.9	0.008	9.53	92.8
	10^{-5}	1.2	174.5	121.7	0.84	58.4	0.007	10.19	87.6
	10^{-6}	1.9	95.2	143.5	0.83	59.6	0.009	5.67	77.3

Table 1. EIS characteristics of C&S corrosion in 1 M HCl in the absence and the presence of ***Tetra-Pz-Ortho*** and ***Tetra-Pz-Para***.

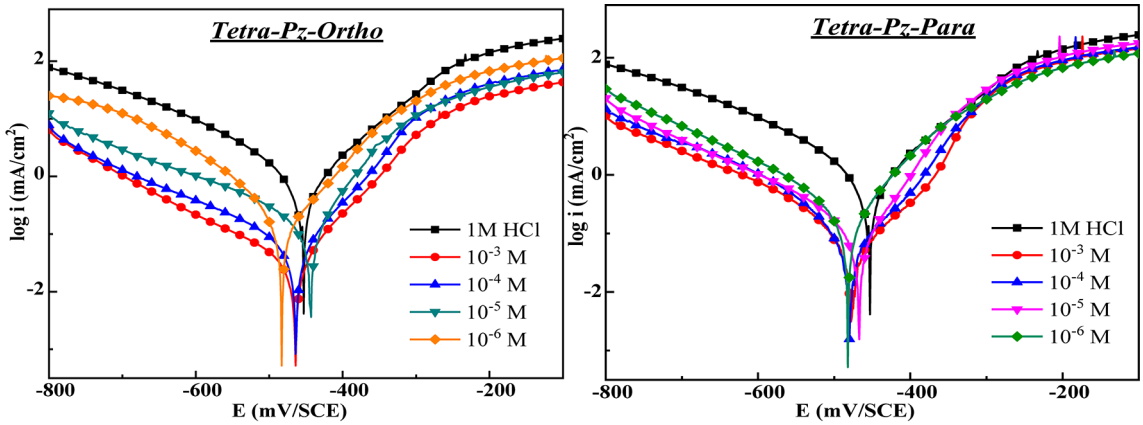

Fig. 4. PDP curves of C&S uninhibited and inhibited with different concentrations of ***Tetra-Pz-Ortho*** and ***Tetra-Pz-Para*** in 1 M HCl at 303 K.

adsorbed at C&S surface[44]. The relaxation time (τ) is also dependent on the values (C_{dl}), which can be found using the following formula[45].

$$\tau = (C_{dl} \times R_p) \tag{5}$$

Depending on the concentration of ***Tetra-Pz-Ortho*** and ***Tetra-Pz-Para***, the relaxation time constant a becomes more significant, which supports a delayed adsorption process time[46]. It is also worth noting that the values of xi-square (χ^2) (Table 1) are very low values in the tested range of concentration, which confirms the proposed circuit[17]. This brings with it the possibility of a blocking of the active sites responsible of the dissolution of C&S in the presence of both ***Tetra-Pz-Ortho*** and ***Tetra-Pz-Para***, in addition to adsorption phenomenon.

These molecular structures might also activate the bond formation with the vacant d-orbitals of Fe atoms at the surface, this character will be most significant for ***Tetra-Pz-Ortho*** than that ***Tetra-Pz-Para***. The molecular structure of the latter easily leads to adsorption by chemisorption or physisorption or both[47]. Furthermore, as stated in the literature[48], this event is proof of the formation of the bond O-Fe, with distinctive donor-acceptor interactions between the Fe unoccupied d-orbitals and the electron pairs (sp^2) of the N-atoms in the amino groups and pyrazole ring.

PDP measurements

PDP plots of C&S in 1 M HCl electrolyte alone and with ***Tetra-Pz-Ortho*** and ***Tetra-Pz-Para*** inhibitors are elucidated in Fig. 4. The deduced parameters from these curves for the different concentrations tested are regrouped in Table 2, namely current density, Tafel slopes, corrosion-potential (noted respectively: catodic-β (β_c), anodic-β (β_a), i_{corr} and E_{corr}). Inhibitory effectiveness based on i_{corr} of each inhibitor was calculated by this Eq:

$$E_{Tafel}\,(\%) = \left(\frac{i_{cor,free} - i_{cor,Inh}}{i_{cor,free}}\right) \times 100 \tag{6}$$

Medium	Conc. (M)	$-E_{corr}$ (mV vs. SCE)	i_{corr} (μA cm^{-2})	$-\beta_c$	β_a	η_{pp} (%)
HCl	Blank	456.3	1104	112	155.4	–
Tetra-Pz-Ortho	10^{-3}	466.0	30.8	156.5	76.6	**97.2**
	10^{-4}	461.9	53.3	151.2	76.0	95.2
	10^{-5}	442.0	114.7	147.5	61.6	89.6
	10^{-6}	483.1	199.3	105.3	85.0	81.9
Tetra-Pz-Para	10^{-3}	477.4	44.2	78.0	88.4	**96.0**
	10^{-4}	478.6	68.6	91.1	71.4	93.8
	10^{-5}	469.2	136.7	143.5	69.3	87.6
	10^{-6}	480.1	266.1	153.2	89.3	75.9

Table 2. Data deducted from Tafel extrapolation of C&S in 1 M HCl uninhibited and inhibited with different concentrations of ***Tetra-Pz-Ortho*** and ***Tetra-Pz-Para*** in 1 M HCl at 303 K.

Medium	Conc. (M)	W_{cor} (mg cm^{-2} h^{-1})	η_W (%)
HCl	Blank	1.552	–
Tetra-Pz-Ortho	10^{-6}	0.314	79.76
	10^{-5}	0.182	88.27
	10^{-4}	0.101	93.49
	10^{-3}	0.071	95.42
Tetra-Pz-Para	10^{-6}	0.367	76.35
	10^{-5}	0.211	86.40
	10^{-4}	0.108	93.04
	10^{-3}	0.079	94.91

Table 3. WL parameters for C&S uninhibited and inhibited with different concentrations of ***Tetra-Pz-Ortho*** and ***Tetra-Pz-Para*** in 1 M HCl at 303 K.

where $i_{cor.free}$ is the corrosion current in uninhibited solution and $i_{cor.inh}$ is the corrosion current in inhibited solution, respectively.

The anodic and cathodic current densities decreased with the progressive addition of ***Tetra-Pz-Ortho*** and ***Tetra-Pz-Para***, revealing that the presence of these inhibitors in an acid medium delayed hydrogen reduction and reduced the anodic dissolution of C&S. Additionally, the cathodic branches appear as parallel lines with increasing inhibitor dose, suggesting that the hydrogen evolution processes remain unchanged when **Tetra-Pz-Ortho** and **Tetra-Pz-Para** are added[49]. The reduction of hydrogen ions at the surface of C&S mostly occurs via a charge transfer process. The parameters obtained by extrapolating PDP graphs are provided in Table 2. It is clear that a decreasing in i_{corr} with an augmentation of concentration of ***Tetra-Pz-Ortho*** and ***Tetra-Pz-Para*** molecules leading to an increasing in η_{pp}(%), which reaching values of 97.2% and 96%, respectively for ***Tetra-Pz-Ortho*** and ***Tetra-Pz-Para***. This shows that at 1 M HCl, the two compounds effectively limit the corrosion of C&S. In the absence of **Tetra-Pz-Ortho** and **Tetra-Pz-Para**, the deviation of the corrosion potential is – 466.0 mV and – 477.3 mV, respectively. In the blank solution, E_{cor} (corrosion potential) is – 456.3 mV. The gap (ΔE_{cor}) is less than 85 mV in both cases, consequently these inhibitors act as mixt-type inhibitors[50]. According to values βa and βc (Tafel slopes anodic and cathodic), it appears that this system evolute by slowing the rate of corrosion without changing the way that metal dissolves[51]. The values of the inhibitive performances recorded from EIS and PDP measurements are closely linked and the comes about for the most part appeared that ***Tetra-Pz-Ortho*** has higher performance than ***Tetra-Pz-Para***.

Weight loss analysis

Concentration effect study

A weight loss (WL) method was carried out to ascertain the specimen's corrosion rate both before and after it was submerged in blank and inhibited solutions. The main objective was to compare the corrosion rates observed before and after immersing the specimen in both blank and inhibited solutions. The experiments were conducted at a temperature of 303 K, during a 6-hours immersion period in both blank (1 M HCl) and inhibited solution, and utilizing various concentrations. Table 3 regrouped the corrosion rate W_{cor} and the calculated inhibition efficiency η_W (%) of ***Tetra-Pz-Ortho*** and ***Tetra-Pz-Para***. Corrosion rates without and with inhibitors (noted W_{cor} and $W_{cor/inh}$) and the corresponding η_W (%) were calculated following the Eqs. 7 & 8:

$$W_{\mathrm{cor}} = \frac{\Delta m}{S \times t} \tag{7}$$

$$\eta_W\,(\%) = \frac{W_{cor} - W_{cor/inh}}{W_{cor}} \times 100 \tag{8}$$

where Δm(in mg), S(in cm^2) and t(in h) are the average weight loss, the entire substrate surface and the duration of the solution immersion, respectively.

The results in Table 3 show that the inhibitory efficacy of the two inhibitors increases with concentration, reaching values of 95.42% and 94.91% respectively for ***Tetra-Pz-Ortho*** and ***Tetra-Pz-Para*** at the optimum concentration. This high efficiency explains the ability for the both inhibitors to adhere to the C&S area, which depends, of course, on the chemical structure of each inhibitory molecule[23]. These inhibitory compounds can be categorized as effective inhibitors of C&S corrosion in a 1 M HCl solution, confirming the spread of an inhibitory layer on the surface by the replacement of aggressive components. Indeed, the structure of these molecules containing aromatic and pyrazole rings with N-atoms and amino groups giving a high electronic density, this facilitated the adsorption of ***Tetra-Pz-Ortho*** and ***Tetra-Pz-Para*** through these actives' centres on the C&S surface. Consequently, this comportment leads to a significantly covering, and thus formation of adsorbed film made up of molecules ***Tetra-Pz-Ortho*** and ***Tetra-Pz-Para*** on the surface of the metal. The aromatic rings' π electron content and the non-binding electrons on N-atoms, as well as the pyrazole forms, they contain in addition to their large size, easily lead to the adsorption of these newly synthesized compounds[52].

Temperature effect study

The temperature is one of the parameters listed in several industrial sector, as a factor affecting on the metal corrosion in acid medium, by acting on the interaction metal/inhibitors. In general, a good inhibitor must be stable, particularly in acid pickling baths, at temperatures of 333 K or more. Moreover, the impact of the variation of this parameter informs on the inhibitory molecules action mechanism through the calculation and interpretation of activation thermodynamic parameters and allows us to access to the typology of adsorption process[52]. In order to prove this, this study was performed in a temperature interval between 303 and 333 K at different concentration tested, during a one-hour immersion period in both blank (1 M HCl) and inhibited solution. The results obtained are reported in Table 4 and show that an increase of T(K) was accompanied by a considerable rise in corrosion rate W_{cor}, giving thus a decrease of the effectiveness η_W(%). The evolution of these last parameters as function of concentration and temperature in the presence of ***Tetra-Pz-Ortho*** and ***Tetra-Pz-Para*** shows (Table 4) that both the molecules acted as effective inhibitors' even at high temperatures for C&S corrosion in 1 M HCl and the effects are both concentration and temperature dependent. It is also obvious from Table 4 that a rise in temperature for each concentration there is slight lowering in the effectiveness η_W(%) and the corresponding values of surface coverage (θ).

The thermodynamic quantities associated to that phenomenon such as activation energy and enthalpy (E_a & ΔH_a) as well as activation entropy (ΔS_a) are following the Eqs. 9 & 10:

T (K)	Conc. (M)	*Tetra-Pz-Ortho*			*Tetra-Pz-Para*		
		W_{cor} ($mg\,cm^{-2}h^{-1}$)	η_W(%)	θ	W_{cor} ($mg\,cm^{-2}h^{-1}$)	η_W (%)	θ
303	*Blank*	1.519	–	–	1.519	–	–
	10^{-6}	0.406	73.3	0.733	0.497	67.3	0.673
	10^{-5}	0.289	81.0	0.810	0.304	80.0	0.800
	10^{-4}	0.179	88.2	0.882	0.217	85.7	0.857
	10^{-3}	0.113	92.6	0.926	0.134	*91.2*	0.912
313	*Blank*	2.737	–	–	2.737	–	–
	10^{-6}	1.094	60.0	0.600	0.971	64.5	0.645
	10^{-5}	0.627	77.1	0.771	0.684	75.0	0.750
	10^{-4}	0.405	85.2	0.852	0.512	81.3	0.813
	10^{-3}	0.278	89.8	0.898	0.266	90.3	0.903
323	*Blank*	4.457	–	–	4.457	–	–
	10^{-6}	1.908	57.2	0.572	1.767	60.4	0.604
	10^{-5}	1.141	74.4	0.744	1.178	73.6	0.736
	10^{-4}	0.812	81.8	0.818	0.975	78.1	0.781
	10^{-3}	0.602	86.5	0.865	0.558	87.5	0.875
333	*Blank*	7.108	–	–	7.108	–	–
	10^{-6}	3.197	55.0	0.550	3.065	56.9	0.569
	10^{-5}	2.089	70.6	0.706	2.108	70.3	0.703
	10^{-4}	1.558	78.1	0.781	1.755	75.3	0.753
	10^{-3}	1.240	82.6	0.826	1.119	84.3	0.843

Table 4. Temperature evolution for each concentration of both ***Tetra-Pz-Ortho*** and ***Tetra-Pz-Para*** in 1 M HCl.

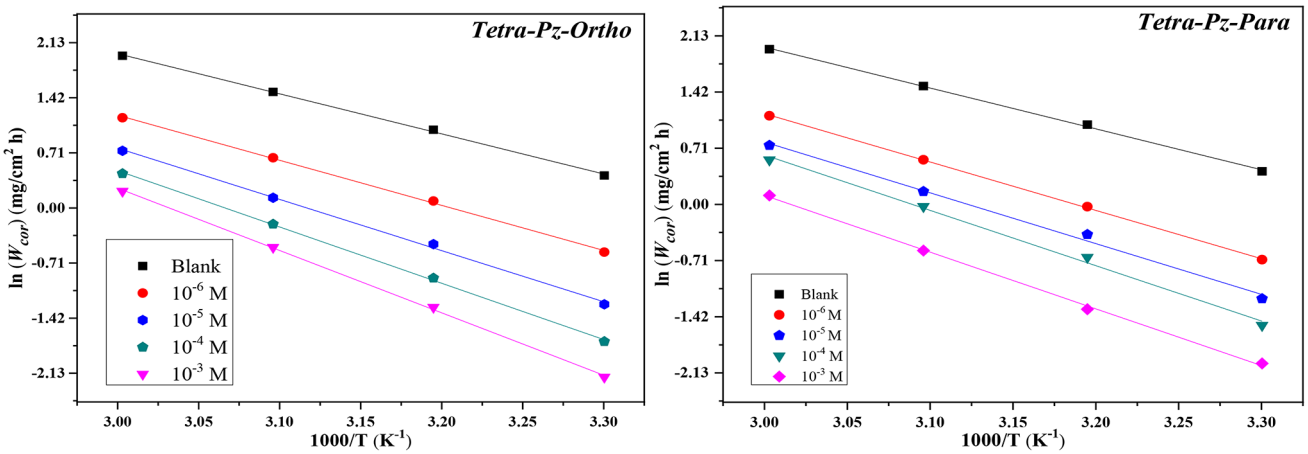

Fig. 5. Arrhenius lines for C&S in 1 M HCl medium in the absence and the presence addition of different concentrations of ***Tetra-Pz-Ortho*** and ***Tetra-Pz-Para.***

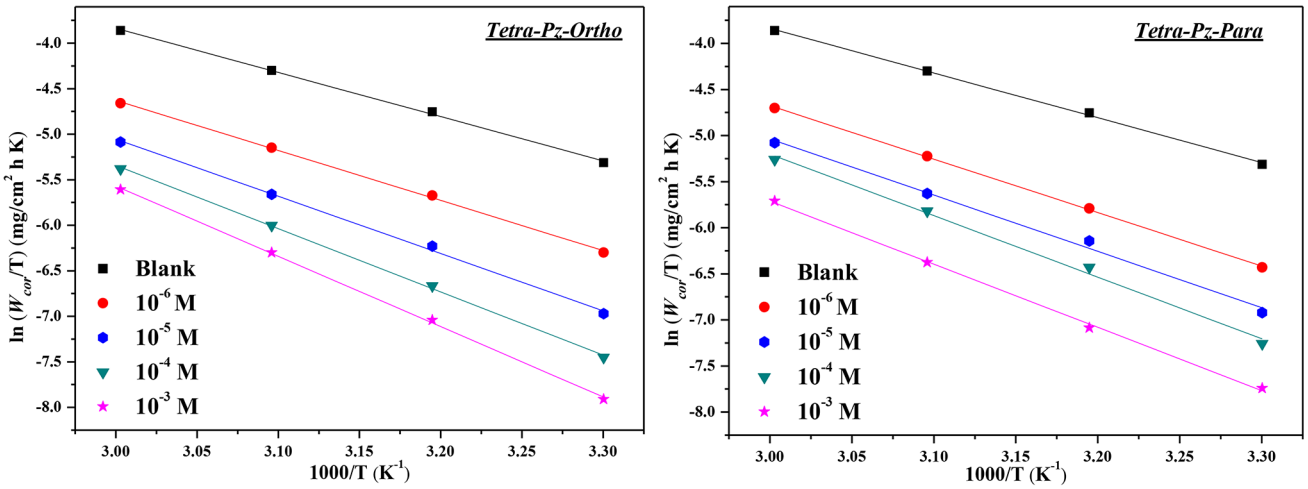

Fig. 6. Variation of ln (W_{cor}/T) as a function of 1000/T the absence and with the presence of different doses of ***Tetra-Pz-Ortho*** and ***Tetra-Pz-Para.***

$$ln\,(W_{cor}) = -\frac{E_a}{RT} + Ln\,(A) \tag{9}$$

$$ln\left(\frac{W_{cor}}{T}\right) = Ln\left(\frac{R}{Nh}\right) + \left(\frac{\Delta S_a}{R}\right) - \left(\frac{\Delta H_a}{RT}\right) \tag{10}$$

Where, A, R and h are constants (pre-exponential constant, gas constant and Plank's constant, respectively) and N is the Avogrado's number. The corrosion rate plot $ln\,(W_{cor})$ for both ***Tetra-Pz-Ortho*** and ***Tetra-Pz-Para*** as function of the inverse of T allow us to calculate E_a (Fig. 5), while the calculation of the thermodynamic quantities ΔH_a and ΔS_a is done on the basis of the equation of Arrhenius (Eq. 10) and the plot of corrosion rate W_{cor} per T ($ln\,(W_{cor}/T)$) as function of the inverse of T (Fig. 6).

The thermodynamic quantities values E_a & ΔH_a and ΔS_a for both the molecules are regrouped in Table 5. The values of the activation energies vary from 48.28 to 66.82 kJ mol^{-1} for ***Tetra-Pz-Ortho*** and from 50.79 to 59.58 kJ mol^{-1} for ***Tetra-Pz-Para***, by increasing the concentration (10^{-6} to 10^{-3} M), while E_a value of the blank solution is of 42.96 kJ mol^{-1}. It is clear, therefore, that E_a values of both the molecules for all tested concentration increase relative to the blank solution. This augmentation of activation energy in the presence of inhibitors is due to a decrease of the dissolution of the C&S and the increase in the energy barrier of the corrosion reaction, i.e. both molecules tested can form an energy barrier to protect the C&S surface vis-a-vis corrosive attack[53].The positive values of ΔH_a for all the concentration tested show the endothermic nature of the dissolution of C&S. In the presence of ***Tetra-Pz-Ortho*** and ***Tetra-Pz-Para***, the values of ΔS_a move toward positive way, by passing from the blank to inhibitory solution and by increasing the concentration, implying the barriers crossing to adsorption for both inhibitors on the metal surface[54]. However, from the Table 5 one noted also that E_a value of inhibitor

Conc. (M)		E_a(kJ mol^{-1})	ΔH_a(kJ mol^{-1})	ΔS_a(J mol^{-1}k^{-1})
Blank		42.96	40.37	-108.34
Tetra-Pz-Ortho	10^{-6}	48.28	45.69	-98.97
	10^{-5}	54.86	52.26	-82.78
	10^{-4}	60.34	57.74	-68.74
	10^{-3}	66.82	64.22	-51.17
Tetra-Pz-Para	10^{-6}	50.79	48.24	-91.70
	10^{-5}	53.38	50.79	-87.05
	10^{-4}	58.12	55.52	-74.22
	10^{-3}	59.58	56.99	-74.06

Table 5. Thermodynamic parameters of activation of C&S in molar HCl without and with addition of ***Tetra-Pz-Ortho*** and ***Tetra-Pz-Para***.

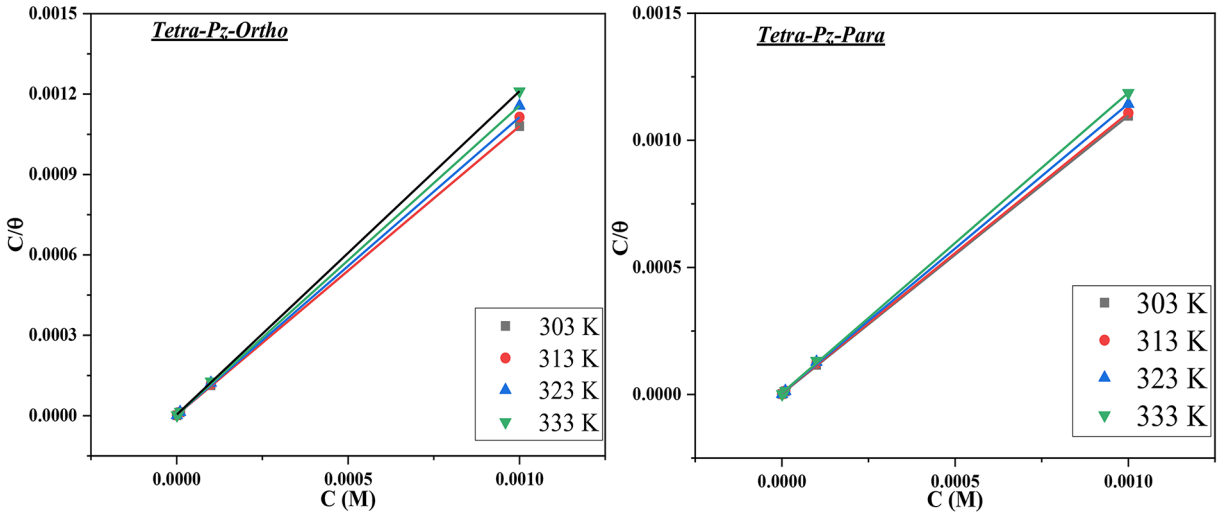

Fig. 7. Langmuir adsorption isotherm for C&S in molar HCl without and with addition of ***Tetra-Pz-Ortho*** and ***Tetra-Pz-Para*** at different temperatures.

Tetra-Pz-Ortho is greater than that of inhibitor ***Tetra-Pz-Para***, at the optimum concentration this indicates that ***Tetra-Pz-Ortho*** has an inhibitory effect more significant than ***Tetra-Pz-Para***,

Adsorption isotherm model

Both the well-known phenomena of adsorption of the organic compounds as corrosion inhibitors at a metal surface are the chemisorption and the physisorption. The chemisorption or chemical adsorption can be linked to the coordination bond formed between d-orbitals of iron atoms and non-bonding electrons of heteroatoms and/or aromatic ring of inhibitory molecules. The physisorption or physical adsorption can be related to the interaction between a charge of tested molecular structure and a charge of iron atoms (electrostatic interactions). Hence, the interfacial adsorption mechanism of the tested molecules as inhibitors can be interpreted on the basis on the both these phenomena. Among the methods used to treat this subject are the adsorption isotherm studies of inhibitors, with the purpose to be highlighted the interfacial interactions process substrate/adsorbate[55]. Based on the recovery rate ($\theta = E_{WL}$ (%)/100) (Table 4) of both ***Tetra-Pz-Ortho*** and ***Tetra-Pz-Para***, we tried the various know isotherms (Langmuir, Freundlich, Temkin …) to find the one that appropriates best for our case. These tests have been done using the gravimetric method in the ranging of the proposed concentration (Table 4) at different temperature (from 303 K to 333 K) as described in Fig. 7. The Langmuir model equation (Eq. 11) provides the best fit to our data, confirming a Langmuir adsorption isotherm for both molecules tested.

$$\frac{C}{\theta} = \frac{1}{K_{ads}} + C \tag{11}$$

Where C and θ are respectively the concentration and the surface coverage of tested inhibitors.

K_{ads} is the adsorption equilibrium−constant, its values will make it possible to determine the ΔG^0_{ads} thermodynamic quantities (Free energies of adsorption) for the different proposed temperature by using the following equation:

	Temp. (K)	K_{ads} (M^{-1})	Slope	R^2	ΔG^0_{ads} (kJ mol^{-1})	ΔH^0_{ads} (kJ mol^{-1})	ΔS^0_{ads} (J $mol^{-1}k^{-1}$)
Tetra-Pz-Ortho	303	420,382	1.07	0.9999	-43.45	-8.84	114.00
	313	359,958	1.11	0.9999	-44.45		
	323	332,185	1.15	0.9999	-45.62		
	333	313,888	1.20	0.9999	-46.86		
Tetra-Pz-Para	303	251,911	1.09	0.9999	-42.13	-10.05	105.50
	313	204,452	1.10	0.9999	-42.95		
	323	186,580	1.13	0.9999	-44.05		
	333	178,930	1.18	0.9999	-45.28		

Table 6. Thermodynamic parameters of adsorption for C&S in 1 M HCl medium without and with addition of ***Tetra-Pz-Para*** and at different temperatures.

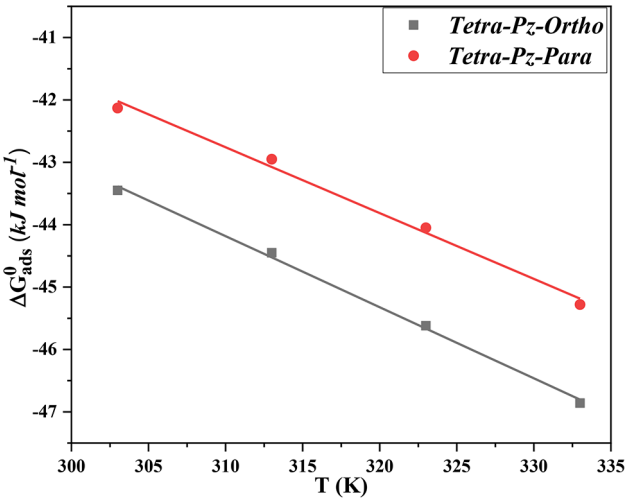

Fig. 8. Variation of ΔG^0_{ads} vs. T for C&S in HCl containing ***Tetra-Pz-Ortho*** and ***Tetra-Pz-Para***.

$$K_{ads} = 0.018 \times exp\left(-\frac{\Delta G^0_{ads}}{RT}\right) \tag{12}$$

The value 0.018 is the inverse of the concentration (55.5 M) of water, R is the molar gas constant, and T (K) is the temperature. Table 6 regroups the main parameters of both the inhibitors, ***Tetra-Pz-Ortho*** and ***Tetra-Pz-Para***, deduced from the plot of the regression line of presented in Fig. 7, with a slope closed to 1 for each temperature tested, confirming thus the Langmuir model adoption process. The issued parameters of adsorption from the Langmuir isotherm (Table 6) are exhibiting a regression coefficient R^2 of 1 for the two molecules. Table 6 shows also that the values of adsorption equilibrium constants K_{ads} are higher and decrease by increasing the temperature for each inhibitor (***Tetra-Pz-Ortho*** and ***Tetra-Pz-Para)***. Generally, the higher the K_{ads} constant, the adsorption of the tested compounds is loud. This result show that the active sites present on the exposed surface have been filled with the molecular structures tested[56]. The ΔG^0_{ads} values, calculated from K_{ads} in accordance with the Eq. (10), of both ***Tetra-Pz-Ortho*** and ***Tetra-Pz-Para*** for each temperature vary between − 46 and − 42 kJ mol^{-1} (Table 6), i.e. less than − 40 kJ mol^{-1}, implying that this process is based on chemical adsorbing, even at high temperatures, which could lead to thin layer adsorbed of these organic molecules on the C&S surface. Indeed, according to the literature[57,58], a value of ΔG^0_{ads} less than − 40 kJ mol^{-1} corresponds to the chemical adsorption, a value ΔG^0_{ads} bigger than − 20 kJ mol^{-1} corresponds to the physical adsorption and an intermediate value thereof can be attributed to a physico-chemical adsorption.

For the other thermodynamic quantities of adsorption (ΔH^0_{ads} *and* ΔS^0_{ads}), they are calculated from the intercept and slop of Fig. 8, i.e. the plot of the free energy of adsorption ΔG^0_{ads} as function temperature, and regrouped in Table 6. The obtained values for the pairs parameters (ΔH^0_{ads};ΔS^0_{ads}) are (-8.84 kJ mol^{-1}; 114 kJ mol^{-1} K^{-1}) and (-10.05 kJ mol^{-1}; 105.50 kJ mol^{-1} K^{-1}) for ***Tetra-Pz-Ortho*** and ***Tetra-Pz-Para***, respectively. The negative values of adsorption enthalpy are in accordance of an exothermic behaviour of adsorption of inhibitors while the positive aspect of adsorption entropy may be related to a process that mainly controlled by the adsorption entropy and describe the significant interaction of the system adsorbate/adsorbent[59]. The adsorption of tested inhibitors is a quasi-substitution process adsorption/desorption of tested inhibitors by the

water molecules at the interface electrode/solution. This is a resultant of the entropy of inhibitor and solvent, with a decrease in entropy of inhibitors and the increase in entropy of solvent[60].

Surface estimation

XPS analysis

The realization of XPS spectra of the protective film on the C&S surface in HCl medium and the analysis of their elemental composition analysis showed that there are the presence of Fe, C, N, and Cl. These XPS spectra were done with an optimum concentration of ***Tetra-Pz-Ortho*** and ***Tetra-Pz-Para***. By doing a practical Shirley-baseline with a combination Gaussian–Lorentzian and basing on an algorithm of non-linear least squares, the deconvolution fitting procedure was accomplished. High-resolution peaks have been achieved for N 1s, C 1s, Fe 2p and Cl 2p core levels for both the inhibitors ***Tetra-Pz-Ortho*** and ***Tetra-Pz-Para*** and they are presented in Fig. 9, while the Data deduced from these spectra are grouped in Table 7. Figure 9 shows the C 1s spectra (a / b) of C&S surface in the presence of ***Tetra-Pz-Ortho***(a) / ***Tetra-Pz-Para***(b), which are deconvoluted peaks into three components respectively at 280.95/284.89, 282.33/296.24 and 284.10/288.47 eV. The first component was attributed to the bonds C–C/C=C/C–H, the secondary attribution related to the bond –C–N can be ascribed to amine group and the last was attributed to the bonds –C=N can be typical of pyrazole ring for both the inhibitors. All these bonds are present in the two molecules tested as inhibitors, justifying their deposit on the surface of C&S.

We note that both the molecules present the same bands (C–C/C=C/C–H, –C–N and –C=N) with position different, and this is equally valid for all other deconvoluted spectra presented in this section. This is evidently can be linked to the elemental composition and the molecular structures of the two inhibitors tested that are nearly the same.

The ***Tetra-Pz-Ortho***(a)/ ***Tetra-Pz-Para***(b) structures (Fig. 1) contain a number of nitrogen-atoms as heteroatoms in pyrazole ring and amine group through which may be adsorbed on the C&S surface, and these active centers could form the basis for a chemisorption process[55]. As to deconvoluting of N 1s spectra of the C&S treated with (a) and (b), they can be fitted into three components, suggesting in the three states a strong presence of Nitrogen N for both the molecules tested: The first one at 252/225 eV 395.37/ 399.31 corresponding to bonds –N–C/–N–N typical to amine group and pyrazole rings, another at 396.08/399.90 eV linked to binding –N=C/N–Fe and can be attributed to the four pyrazoles forming the two molecules and the last one at 397.20/ 400.91 may be due to formation of ammonium ions.

The deconvoluted peaks Cl 2p spectra (Fig. 9 Cl 2p, (a) / (b)) show that Cl atoms are there on C&S surface, giving two components at 194.41 / 198.10 eV and 196.02/ 200.07 eV for ***Tetra-Pz-Ortho***(a)/ ***Tetra-Pz-Para***(b), respectively, corresponding to ($FeCl_2$, $FeCl_3$) and Aromatic Chlorine. In fact, core level of Cl can be fitted on two doublets Cl $2p_{3/2}$ and Cl $2p_{1/2}$ (spin–orbit-spliting), respectively, with a peak Cl $2p_{3/2}$ of a binding energy of 194.41 / 198.10 eV which can be attributed to the bond Cl–Fe in $FeCl_3$. They are might be a possibility to formation of an aromatic Chlorine in the presence of $FeCl_3$[61,62].

As presented in Table 7; Fig. 9, the deconvolution of spectra Fe 2p for the treated C&S surface with ***Tetra-Pz-Ortho***(a)/ ***Tetra-Pz-Para***(b) in at the optimum concentration features four components for each molecule. The first three peaks correspond to a deconvolution of the high-resolution Fe $2p_{3/2}$ and the fourth to Fe$2p_{1/2}$ spectra, as described earlier[63]. The peak at the position of 710.91/710.91 eV for ***Tetra-Pz-Ortho***(a)/ ***Tetra-Pz-Para***(b), respectively, may be related to Fe^{3+} ions form of oxide Fe_2O_3 and hydroxide FeOOH[64,65]. The second deconvoluted peak appear at 712.88/712.99 eV and can be attributed to $FeCl_3$ and to the hydroxide FeOOH. This result shows that the oxides formation is always there despite appropriate treatment of C&S specimens before use to XPS analysis. An increase of ferric ions (Fe^{3+}) amount compared to metal amount (Fe^0), can probably contribute to improving of C&S surface resistance in HCl medium, by building cohesive layer, which can preserve and minimize the corrosion process that precedes. This can be regarded as diminution of C&S dissolution and increasing the C&S substrate corrosion resistance by adding the inhibitors[66]. Lastly, the last peak at 724.59/724.08 eV accredited to the deconvolution peak Fe $2p_{1/2}$ and could also be accredited to the Fe (III) state. All these results show the deposition of inhibitors film of molecules tested (***Tetra-Pz-Ortho***(a)/ ***Tetra-Pz-Para***(b)) on the C&S surface.

SEM analysis

Figure 10(a-d) shows SEM (Scanning Electron Microscopy) images of the C&S specimen, which give four different facets of tested specimen: bare metal surface (a), in the blank solution (b) and in presence of both the molecules ***Tetra-Pz-Ortho*** and ***Tetra-Pz-Para*** (c&d). Figure 10(a) represents the surface of C&S before subjection to the corrosive electrolytes, which show a C&S surface relatively smoother. Figure 10(b) shows the aggressive attack of HCl acid on the surface C&S, which appears sorely destructed and shows lot of irregularities. The last Figs (Fig. 10c&d) show the images of surface morphology after the addition of ***Tetra-Pz-Ortho*** and ***Tetra-Pz-Para***, which have changed significantly the surface that become more smoothly and the damages have been reduced. This show that the metal surface condition remained intact with a surface deposit process of an inhibitors film adsorbed, formed by the molecular components of ***Tetra-Pz-Ortho*** and ***Tetra-Pz-Para.*** As shown in the XPS analysis section, the presence of ***Tetra-Pz-Ortho*** and ***Tetra-Pz-Para*** addition in the acid solution promotes improving the metal morphological texture, which become smoother as looking those SEM images (Fig. 10c&d), confirming thus the development of an inhibitory adsorbed coating on the surface of C&S, which can play the role of the barrier among the C&S and acid solution.

UV-visible

A UV-Visible spectra analysis for the 1 M HCl solution in the presence of ***Tetra-Pz-Ortho*** and ***Tetra-Pz-Para*** after gravimetric test at the optimum concentration has been investigated so that we can see complexing power

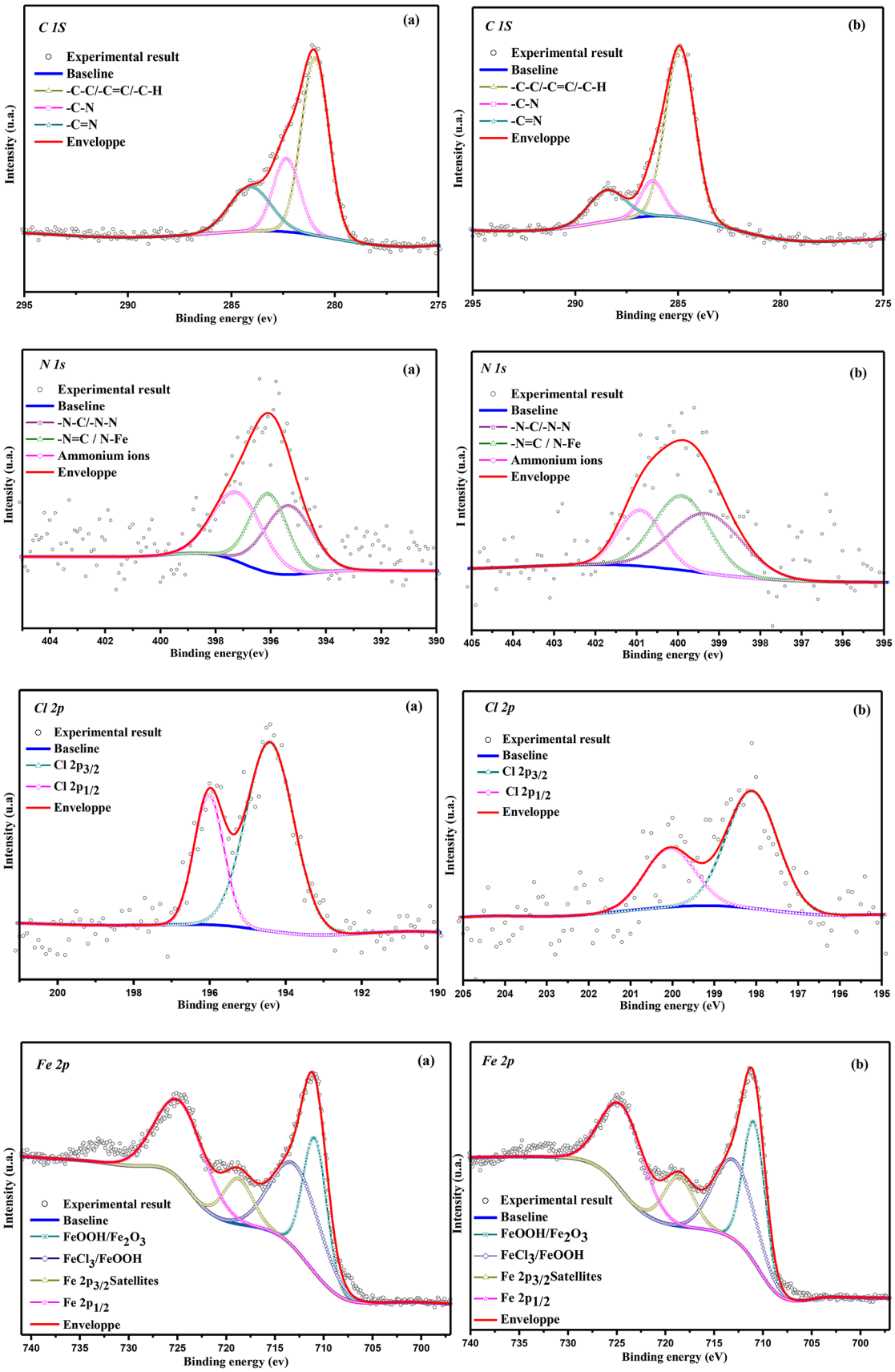

Fig. 9. XPS spectra detailed for C&S surface after being immersed in 1 M HCl with an optimum concentration of (**a**): ***Tetra-Pz-Ortho***, (**b**): ***Tetra-Pz-Para.***

	C 1s		*N* 1s		Cl 2p		Fe 2p	
	Position (eV)	Attribution	Position (eV)	Attribution	Position (eV)	Attribution	Position (eV)	Attribution
(a)	280.95	C–C/C=C/C–H	395.37	–N–C/–N–N	194.41	Cl $2p_{3/2}$	710.91	Fe_2O_3/FeOOH
	282.33	–C–N	396.08	–N=C/N–Fe	196.02	Cl $2p_{1/2}$	712.88	$FeCl_3$/FeOOH
	284.10	–C=N	397.20	Ammonium ions	–	–	718.79	Fe $2p_{3/2}$ Satellites
							724.59	Fe $2p_{1/2}$
(b)	284.89	C–C/C=C/C–H	399.31	–N–C/–N–N	198.10	Cl $2p_{3/2}$	710.91	Fe_2O_3/FeOOH
	286.24	–C–N	399.90	–N=C/N–Fe	200.07	Cl $2p_{1/2}$	712.99	$FeCl_3$/FeOOH
	288.47	–C=N	400.91	Ammonium ions	–	–	718.62	Fe $2p_{3/2}$ Satellites
							724.08	Fe $2p_{1/2}$

Table 7. XPS analysis results for C&S surface after being immersed in 1 M HCl with an optimum concentration of (a): ***Tetra-Pz-Ortho***, (b): ***Tetra-Pz-Para***.

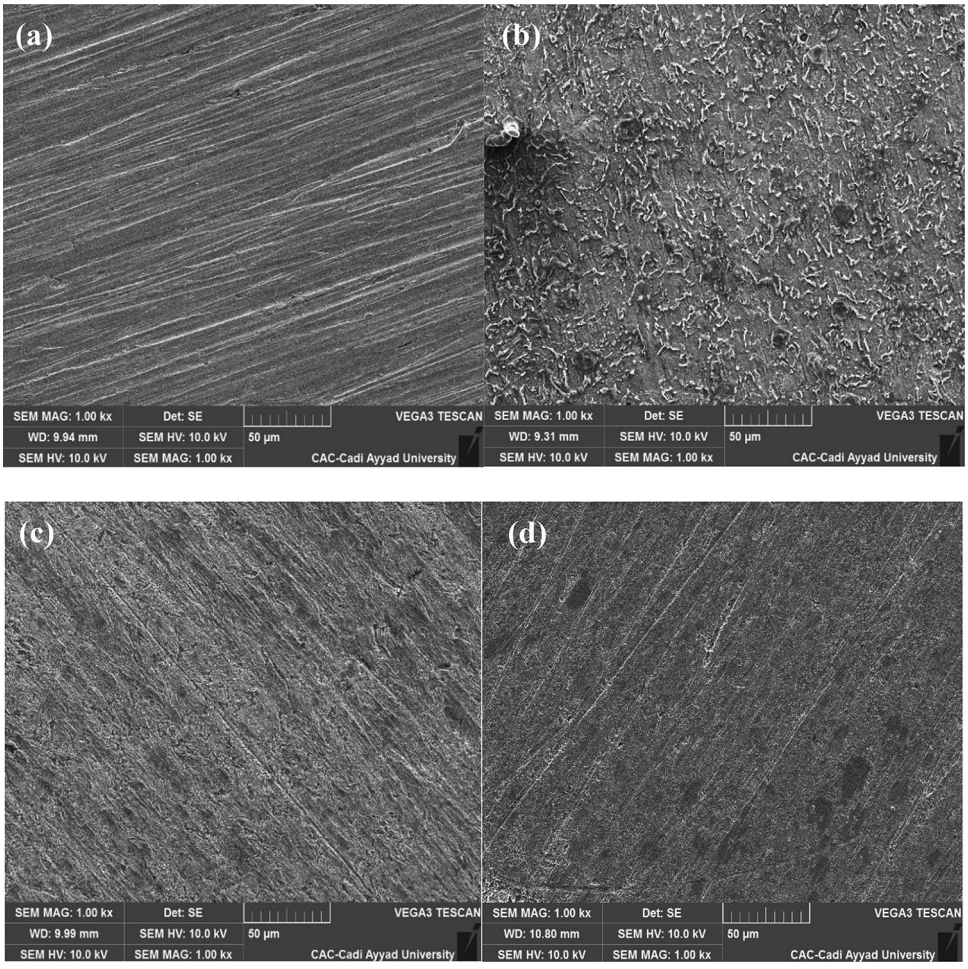

Fig. 10. SEM images of C&S immersed in 1 M HCl, immersed in 1 M HCl + ***Tetra-Pz-Ortho*** and ***Tetra-Pz-Para***, respectively.

of these inhibitors with ferrous ions[67]. Figure 11 shows the UV–visible spectra of a and b in HCl before and after immersion of C&S plates. In both tested cases, it is noted that after immersion of C&S, the maximum wavelengths position (λ_{max}) has changed slightly for ***Tetra-Pz-Ortho*** (first band (212, 213 nm); second band (274,276)), while, in the case of ***Tetra-Pz-Para***, this displacement somewhat bigger (from 252 to 258 nm and from 218 to 223 nm). Generally, these bands in such positions are characteristic of the electronic transitions n → $\pi^*/\pi \rightarrow \pi^*$ of tested molecular structures, obviously with a charge transfer. These finding indicates that these two molecules have complexing character towards the ferrous -ions (Fe^{2+})[68], more significant in the case of (b). In that respect, it may be suggested that it initially had solubility of steel in the solution and the addition of

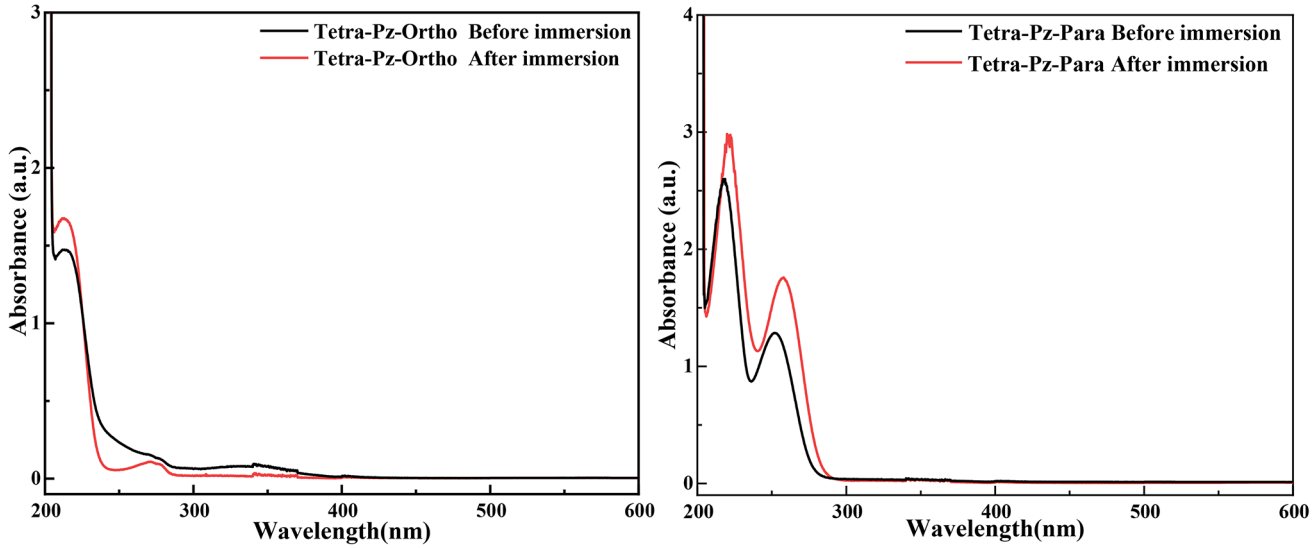

Fig. 11. UV-vis spectra of (***Tetra-Pz-Ortho*** and ***Tetra-Pz-Para)*** / HCl solution before and after soaking of C&S.

inhibitors leads probably to a complexation. Also, the presence of both ***Tetra-Pz-Ortho*** and ***Tetra-Pz-Para*** in the treated acid solution can help minimize the dissolved ferrous ions (Fe^{2+}) by complexing process[69].

Theoretical and computational approach

DFT analysis

Chemical reactivity investigation of organic molecules optimized in their geometry form the most stable is generally characterized by the calculation of global and local reactivity descriptors. The values of these descriptors allow to interpret the theoretical approach of these molecules and to better understanding of interfacial mechanisms of corrosion[68,70]. The two molecules tested ***Tetra-Pz-Ortho*** and ***Tetra-Pz-Para*** can protonate in the HCl medium[62,71]. Using Marvin Sketch software[72], all the distributions of protonated forms as a function of pH (0 to 14) were presented, in order to identify the atom or atoms most likely to bind the H^+ proton. Figure 12(a&b) illustrate the favourable location for protonation that was found to be accessible in ***Tetra-Pz-Ortho*** structure at different sites N6, N35, N36, N37, N65 with a percentage of 99.95% and ***Tetra-Pz-Para*** at the N45, N46, N47, N48 sites with a percentage of 99.90%. The structural chemical reactivity may be influenced by this protonation in both ways, by giving new electronic distribution for two tested molecules ***Tetra-Pz-Ortho*** and ***Tetra-Pz-Para.***

The neutral and protonated forms of molecular structures tested, ***Tetra-Pz-Ortho*** and ***Tetra-Pz-Para***, have been optimized using the density functional theory method (DFT) and both skeleton forms are illustrated in Figs. 13 and 14. The main quantum chemical parameters have been determined basing on Gaussian software (09 W)[33] and were collected in Table 8. These parameters play a significant role in the determination of reactions between the interacting elements. Figures 13 and 14 illustrated the density distributions (HOMO and LUMO), which are well distributed on all neutral and protonated forms for two tested molecules.

For the neutral forms, both molecules have a similar distribution of electron density (Fig. 13). The density relative to HOMO is mainly located on the pyridine ring of compound ***Tetra-Pz-Ortho*** and the benzene ring of compound ***Tetra-Pz-Para***, and includes attached nitrogen atoms and pyrazole rings. LUMO is distributed only on the pyridine ring and the benzene ring. Thus, both compounds tend to interact with the metal surface through electronic transfer. However, the data obtained from the chemical descriptors (Table 8) show that compound ***Tetra-Pz-Ortho*** exhibits higher reactivity than compound ***Tetra-Pz-Para***. Indeed, the energy value of the $\Delta E_{(HOMO-LUMO)}$ of ***Tetra-Pz-Ortho*** is the lowest. The energy values of HOMO and LUMO (-3.800 eV and − 0.623 eV respectively) are lower indicating an ease in both donating and accepting electrons at the unoccupied d orbital of the metal. The calculated value of the fraction of electrons transferred ΔN of ***Tetra-Pz-Ortho*** suggests the possibility of electron transfer between the inhibitor molecule and the metal, likewise, the electrophilic power ($\omega = \frac{\chi^2}{2\eta}$) indicates its tendency to acquire free electrons from the metal and its ability to bind strongly by electron transfer. Moreover, depending on the values of chemical hardness (η) (Table 8) and corresponding softness ($1/\eta$), ***Tetra-Pz-Ortho*** will be more reactive. Its rather high value of deducted softness, compared to that of ***Tetra-Pz-Para***, shows its strong adsorption to the iron surface. This suggests that the inhibitory power of two molecules is not the same, the compound ***Tetra-Pz-Ortho*** tends to interact better and therefore a strong adsorption towards the surface.

In fact, most atomic sites are involved in electron donation and/or acceptance, with the donation effect taking place via centers HOMO, and the acceptance effect taking place via atoms LUMO of electrons from electron-donor centers, namely the orbitals occupied of C&S surface[73].

Figure 14 illustrates the protonated forms (the ***Tetra-Pz-Ortho(5 H^+)*** and ***Tetra-Pz-Para(4 H^+)*** states), which gave new electron density distributions differing from ***Tetra-Pz-Ortho(5 H^+)*** to ***Tetra-Pz-Para(4 H)*** for

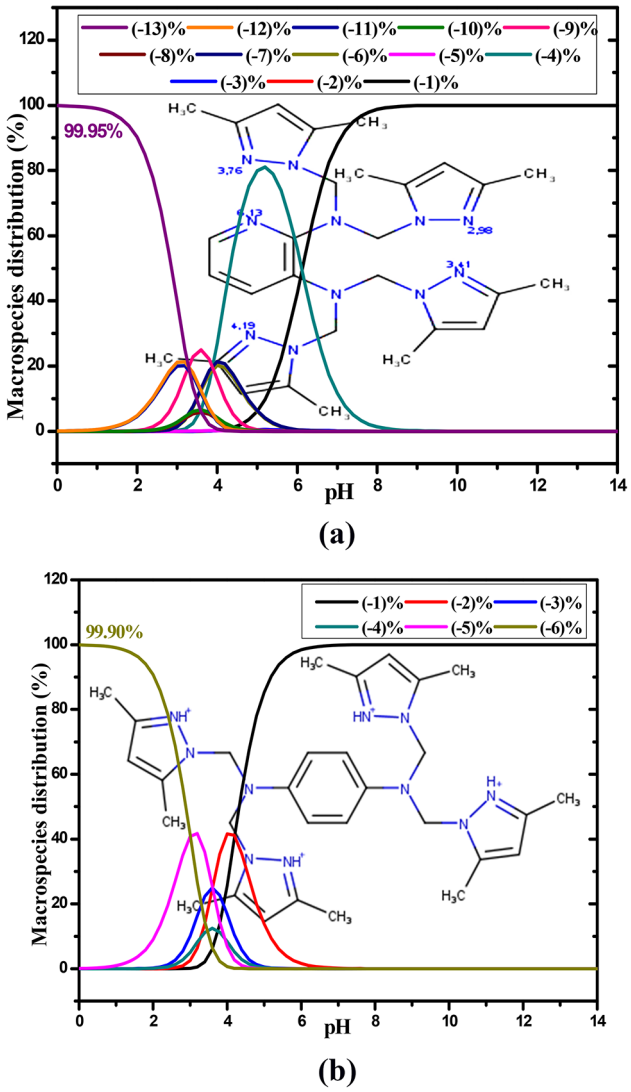

Fig. 12. (**a**) Macrospecies distribution of protonated form of ***Tetra-Pz-Ortho*** (% protonation vs. pH distribution). (**b**) Macrospecies distribution of protonated form of ***Tetra-Pz-Para*** (% protonation vs. pH distribution).

both LUMO and HOMO density. The HOMO density distribution occupies the pyrazole ligands for ***Tetra-Pz-Ortho(5 H⁺)***, while for ***Tetra-Pz-Para(4 H⁺)*** it occupies the benzene center and its vicinity. The LUMO density distribution occupies the pyrimidine center for ***Tetra-Pz-Ortho(5 H⁺)*** and the pyrazole ligands for ***Tetra-Pz-Para(4 H⁺)***. Furthermore, as shown in Table 8, the protonation of these optimized molecules leads to a decrease in the electron-donating effect due to lower E_{HOMO} and ΔN_{110} values. On the other hand, lower E_{LUMO} values for both compounds have boosted the electron-accepting impact.

Mulliken population analysis

To further estimate the inhibitory efficiency of the two synthesized molecules ***Tetra-Pz-Ortho*** and ***Tetra-Pz-Para***, in neutral and pronated form, the distribution of net charges on all of their atoms was calculated using Mulliken's population analysis (MPA), and processed using the B3LYP/6-31G(d, p) basis. This charge distribution is shown in color in Fig. 15 where the more bleu-colored atoms represent the more negatively charged atoms, while the other colored atoms represent some less negatively charged atoms and more positively charged atoms. According to this figure, we note that the atoms of the two molecules have close values, negative charges are located mainly on the nitrogen atoms, the carbon atoms turned out to be positive (with significant negative charge for the carbons methyl) while all protons have a positive charge. Indeed, the atoms carrying positive charges can be described as sites with a certain capacity to receive charges from the (d) orbital of the iron in order to generate a feedback band. In contrast, the lone pair of electrons (negative charges) carried by oxygen atoms is a source of charge capable of donating electrons to iron atoms. Figure 15 shows that the highest negative charges are linked to the Nitrogen numbered N(6 ,10, 11, 25, 30, 36, 65, 78) and to Carbon number C(46, 42, 50, 58, 72) for ***Tetra-Pz-Ortho*** C(43, 47, 53, 57, 65, 69, 73) and for the ***Tetra-Pz-para*** molecule the Nitrogen atoms

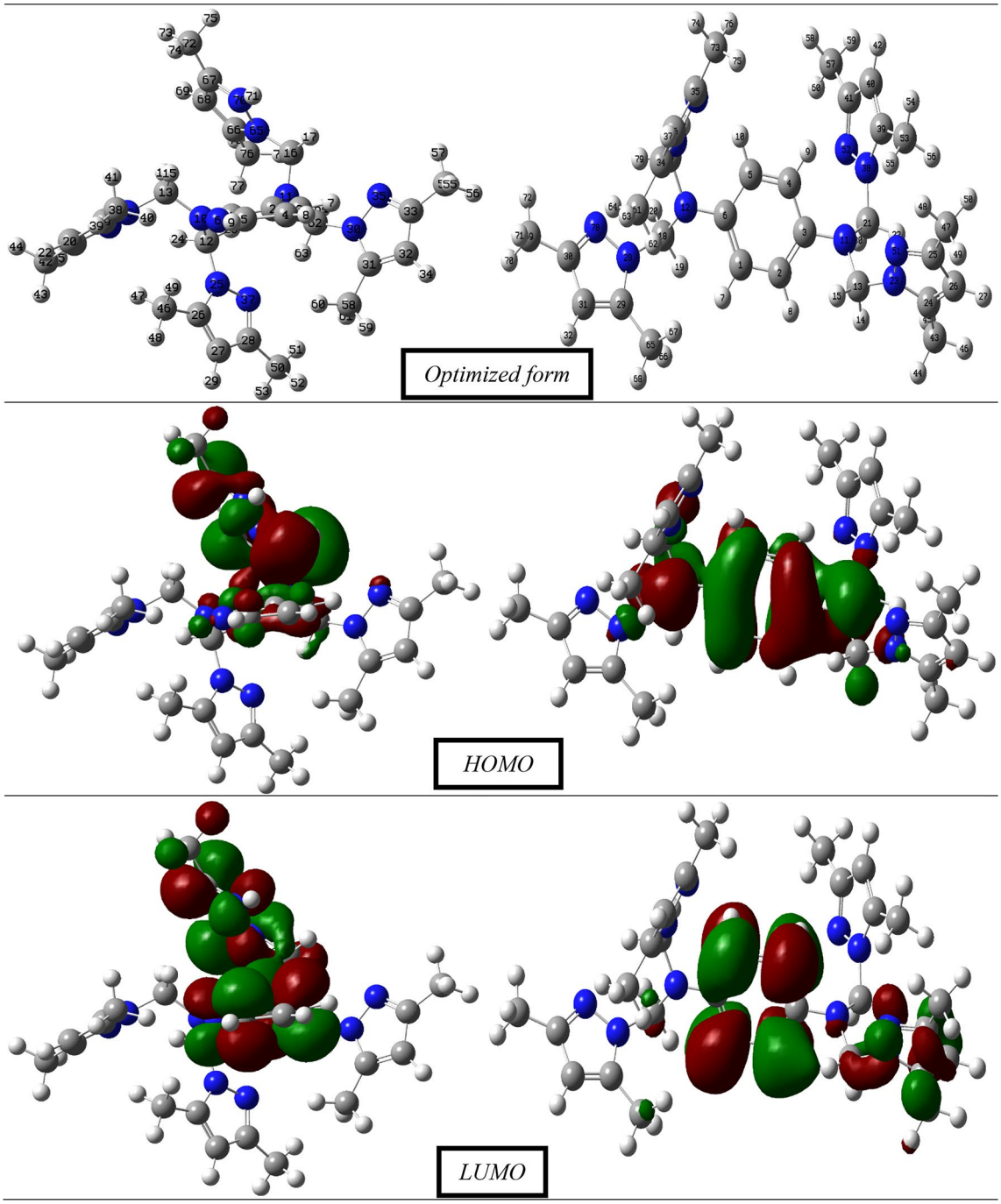

Fig. 13. Optimized molecular structure and Frontier molecular orbitals (HOMO and LUMO) of ***Tetra-Pz-Ortho*** and ***Tetra-Pz-Para***, as neutral molecules.

numbered N(11, 12, 23, 28, 33, 38) and to Carbon number C(43, 47, 53, 57, 65, 69, 73). These results imply that these compounds have electron-donating active sites (lone pair of electrons) towards the vacant (d) iron orbital with the possible formation of a coordination bond. In addition, the presence of positive charges on other atoms suggests the existence of potential locations where these substances are able to receive electrons from the Fe-surface[74]. This electron transfer process contributes to the formation of a feedback bond between the inhibitor molecules and the metal surface[75]. Consequently, the atoms of both the ***Tetra-Pz-Ortho*** and ***Tetra-Pz-Para*** molecules in their neutral forms are a little rich in electrons, in particular their nitrogen atoms. It can be deduced that the two molecules present more favored sites for electrophilic attacks. Finally, it has to be noted that the interactions acceptor/donor of electrons between the metal-atoms of surface and active sites of the ***Tetra-Pz-Ortho*** and ***Tetra-Pz-Para*** molecules can be overall attributed to an adsorption process. The distribution of net charges on all of their atoms (MPA) for the protonated form of ***Tetra-Pz-Ortho*** and ***Tetra-Pz-Para*** are presented in Fig. 16. Except for the N-atoms of amine groups in the two molecules tested, the other atoms, which had a

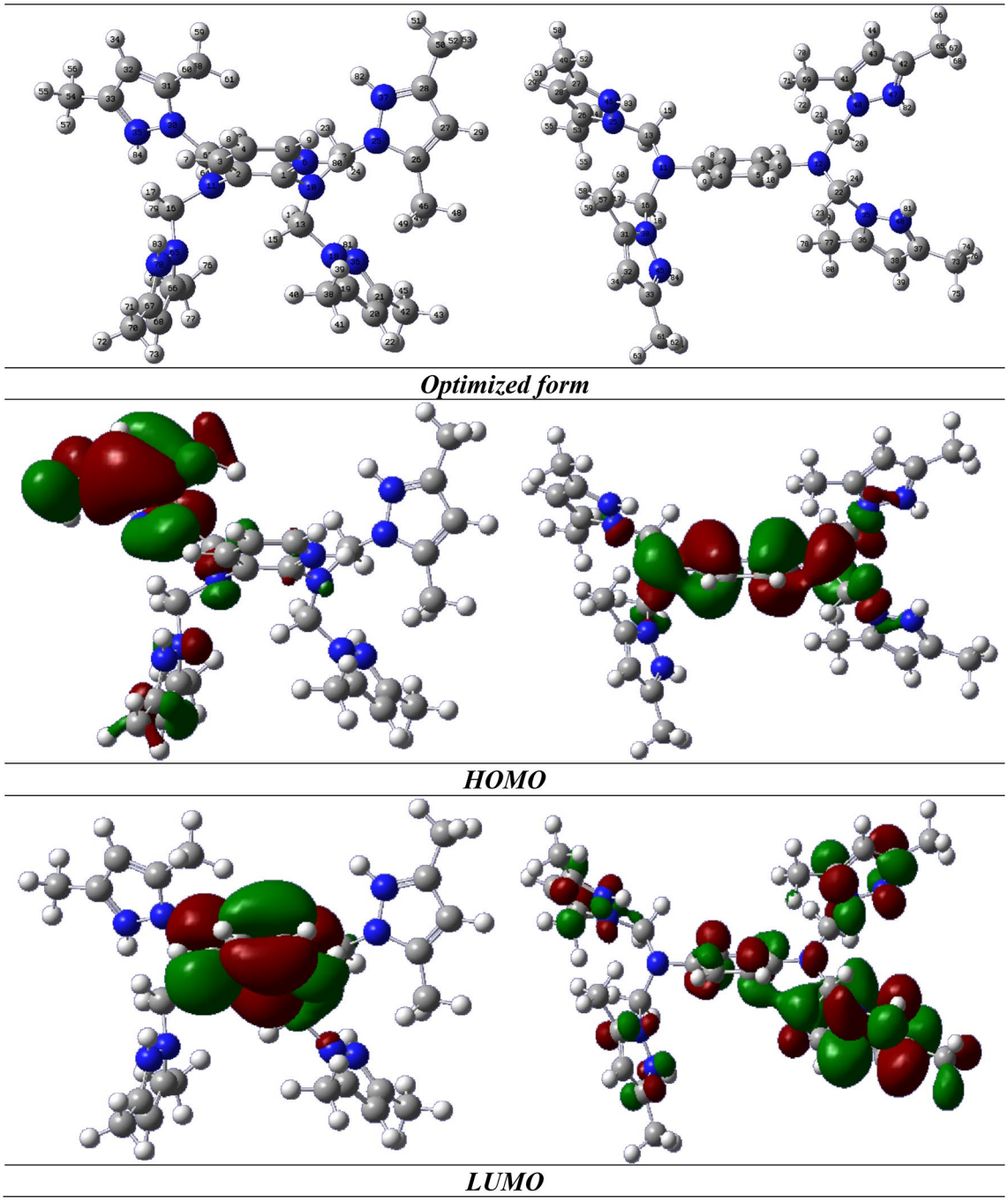

Fig. 14. Optimized molecular structure and frontier molecular orbitals (HOMO and LUMO) of ***Tetra-Pz-Ortho*** and ***Tetra-Pz-Para***, into protonated forms.

very negative charge in the neutral form of these molecules, became less negative in the protonated form, this seeming thus conform with DFT method results.

Monte Carlo and molecular dynamic simulations study

Monte Carlo (MC) and molecular dynamics (MD) simulations methods have been widely used to understand the interaction and adsorption behavior of an inhibitor on the metal surface. In the present work, to fully understand the behavior of the two ***Tetra-Pz-Ortho*** and ***Tetra-Pz-Para*** investigated molecules (in their neutral and protonated form) with respect to the Fe surface, MD and MC simulations were realized in the presence of all the concerned species, water molecules, H_3O^+ and Cl^- in order the mimic the real corrosive environment. The most stable low energy adsorption configurations (side and top views) of the ***Tetra-Pz-Ortho*** and ***Tetra-Pz-Para*** inhibitor molecules on Fe (110) surface are presented in Fig. 17. As is seen from this figure, we notice that the two inhibitors are adsorbed nearly parallel to the Fe (110) surface (both in the gas or in the aqueous medium)

Quantum parameters	Tetra-Pz-Ortho (neutral form)	Tetra-Pz-Para (neutral form)	Tetra-Pz-Ortho ($5\ H^+$)	Tetra-Pz-Para ($4\ H^+$)
$E_{LUMO}(eV)$	-0.623	0.123	-16.027	-10.721
$E_{HOMO}(eV)$	-3.800	-5.157	-19.681	-16.219
$\Delta E\ (eV)$	3.177	5.280	3.653	5.497
$IP = -E_{HOMO}(eV)$	3.800	5.157	19.681	16.219
$EA = -E_{LUMO}(eV)$	0.623	-0.123	16.027	10.721
$\chi = \frac{I+A}{2}\ (eV)$	2.211	2.517	17.854	13.470
$\eta = \frac{I-A}{2}\ (eV)$	1.588	2.640	1.827	2.749
μ (Debye)	5.086	5.398	3.080	4.238
$\Delta N = \frac{\chi Fe - \chi\ inh}{2(\eta Fe - \eta inh)}$	1.636	0.868	-2.970	-1.176
Total energy	-47060.931	-46627.056	-47110.20	-46844.88

Table 8. Calculated quantum chemical parameters of ***Tetra-Pz-Ortho*** and ***Tetra-Pz-Para*** neutral and protonated forms.

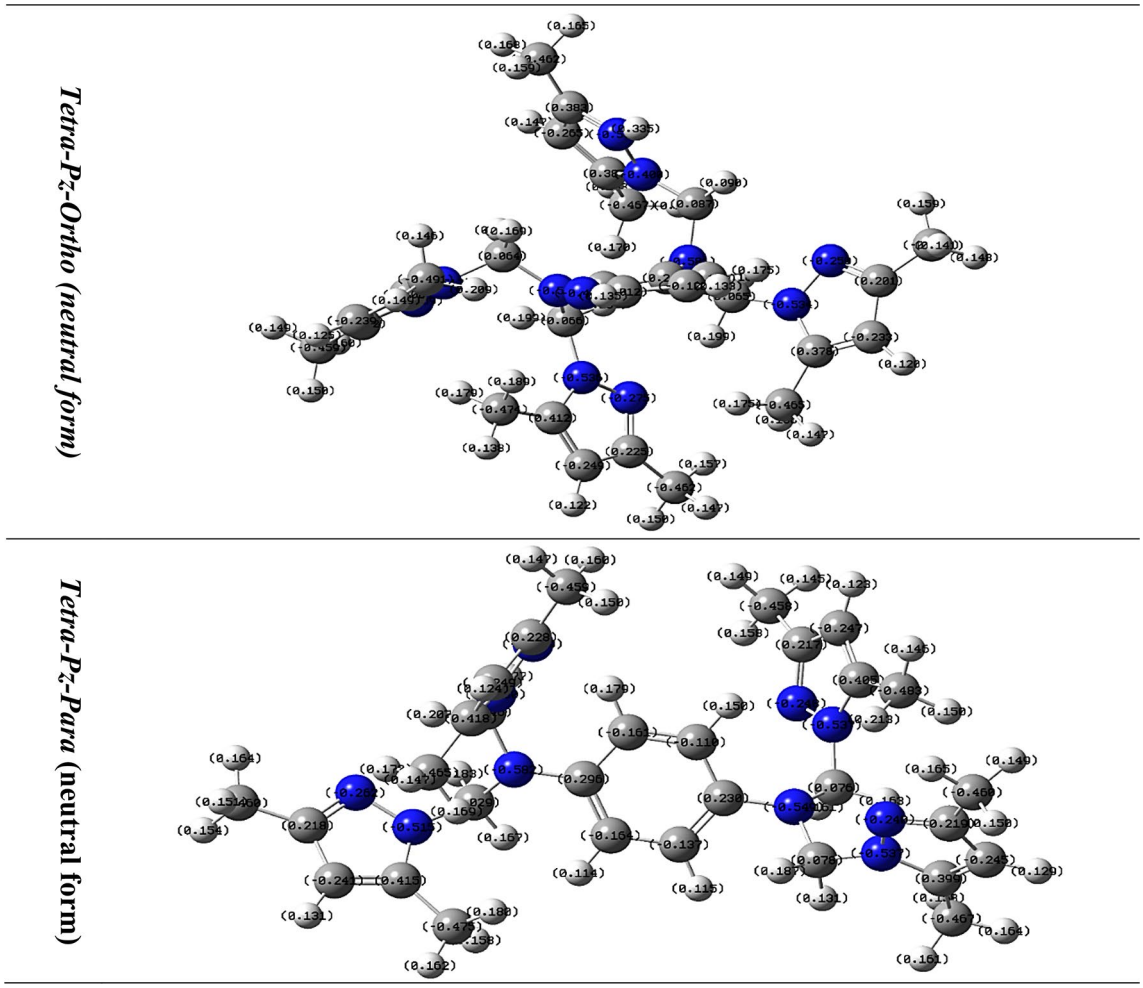

Fig. 15. Mulliken atomic charge distribution of ***Tetra-Pz-Ortho*** and ***Tetra-Pz-Para*** of neutral forms in DFT optimized geometry.

with a maximum contact which promotes better interaction and subsequently better coverage of the surface. The values for the outputs and descriptors of the MC simulations are listed in Table 9. This table provides some important parameters as: total energy, adsorption energy, rigid adsorption energy and deformation energy. The high negative values obtained confirms the stable and stronger adsorption amongst the studied molecules ***Tetra-Pz-Ortho*** and ***Tetra-Pz-Para*** and the Fe surface. However, the corrosion inhibition efficiency of our proposed

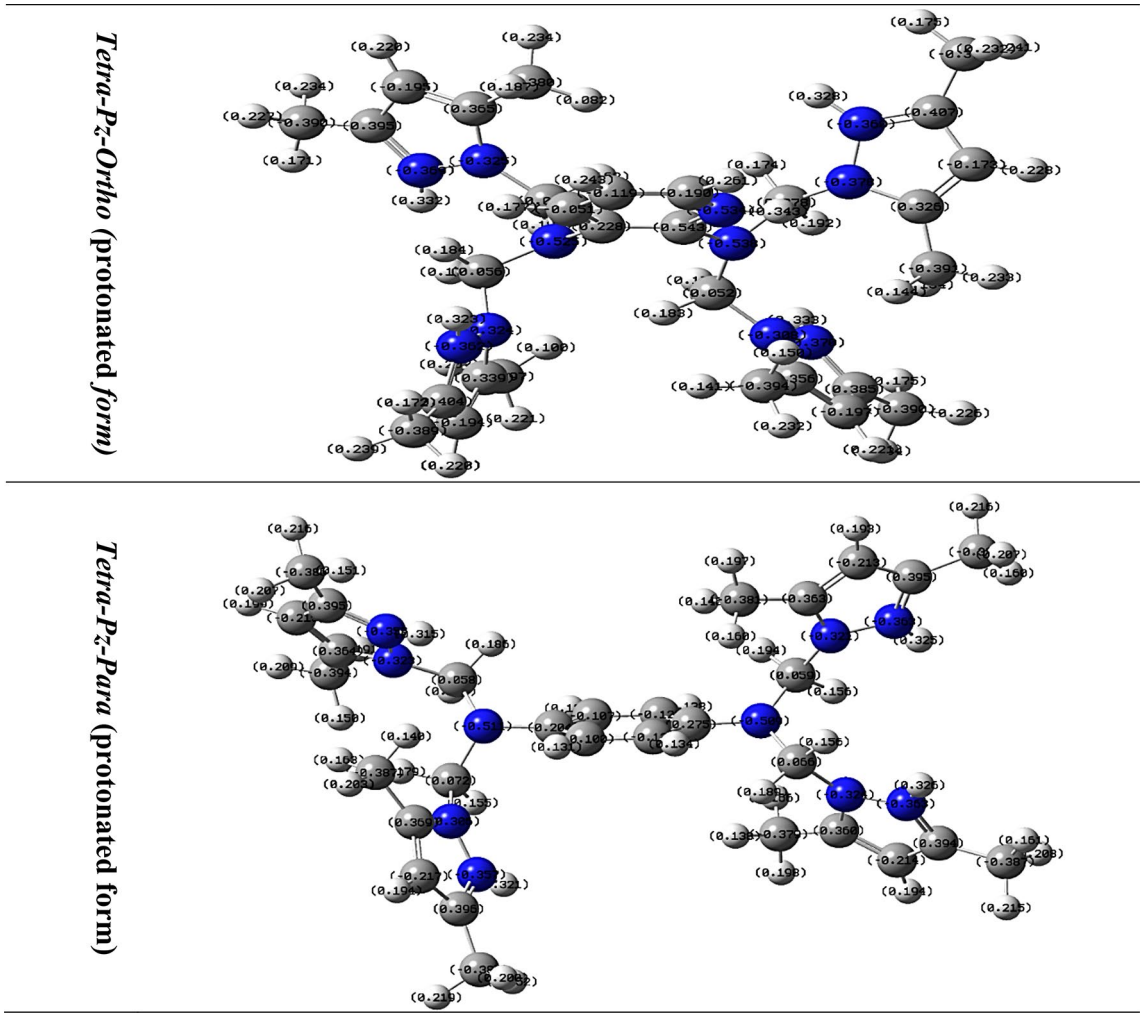

Fig. 16. Mulliken atomic charge distribution of ***Tetra-Pz-Ortho*** and ***Tetra-Pz-Para*** of protonated forms in DFT optimized geometry.

inhibitors varies from one form to another and the ranking order is given as: ***Tetra-Pz-Ortho*** > ***Tetra-Pz-Para***, the ordering also corroborates the protonated forms. This result confirms what was found experimentally.

It is apparent that in the case of the two molecules, the adsorption is generally provided through the nitrogen heteroatoms of the five-membered aromatic rings and π-electrons. The interaction power is improved by the presence of five-membered rings which contain nitrogen atoms. Nitrogen heteroatoms increase the electronic distributions density of the molecule and promote a chemisorption which stabilized also by the free electron pairs. This promotes a strong interaction which makes the molecule more stable on the Fe surface and gives better inhibition.

The inhibitor ***Tetra-Pz-Ortho*** is connected with its four five-membered aromatic rings and exhibiting a more and near-flat adsorption orientation on the Fe surface, in that way, it covers more surface. Similarly, from the data in Table 10, the binding energies of the studied molecules are very high and positive whether in its neutral or protonated state which suggest the high stability of the adsorbed inhibitors.

Radial distribution function

The Radial Distribution Function (RDF) g(r)[76] is an effective structural quantity which describes how the density varies as a function of the distance to a particle of reference. The atomic RDF g(r) shows peaks corresponding to the inter-atomic distances existing in the material. It allows for a direct analysis of the inter-atomic distance and atomic displacements. For our systems, RDF g(r) is useful to estimate the bond length between the atoms of ***Tetra-Pz-Ortho*** and ***Tetra-Pz-Para*** inhibitors and iron. More, it allowed us to conclude the types of bonds formed. The RDF analyzed from the MD results of ***Tetra-Pz-Ortho*** and ***Tetra-Pz-Para*** is graphically presented in Fig. 18. This figure shows that all the bond length of Fe and atoms are less than 3.5 Å (for both ***Tetra-Pz-Ortho*** and ***Tetra-Pz-Para*** atoms), so a chemisorption interaction can occur between the atoms of these two molecules and that of the C&S surface.

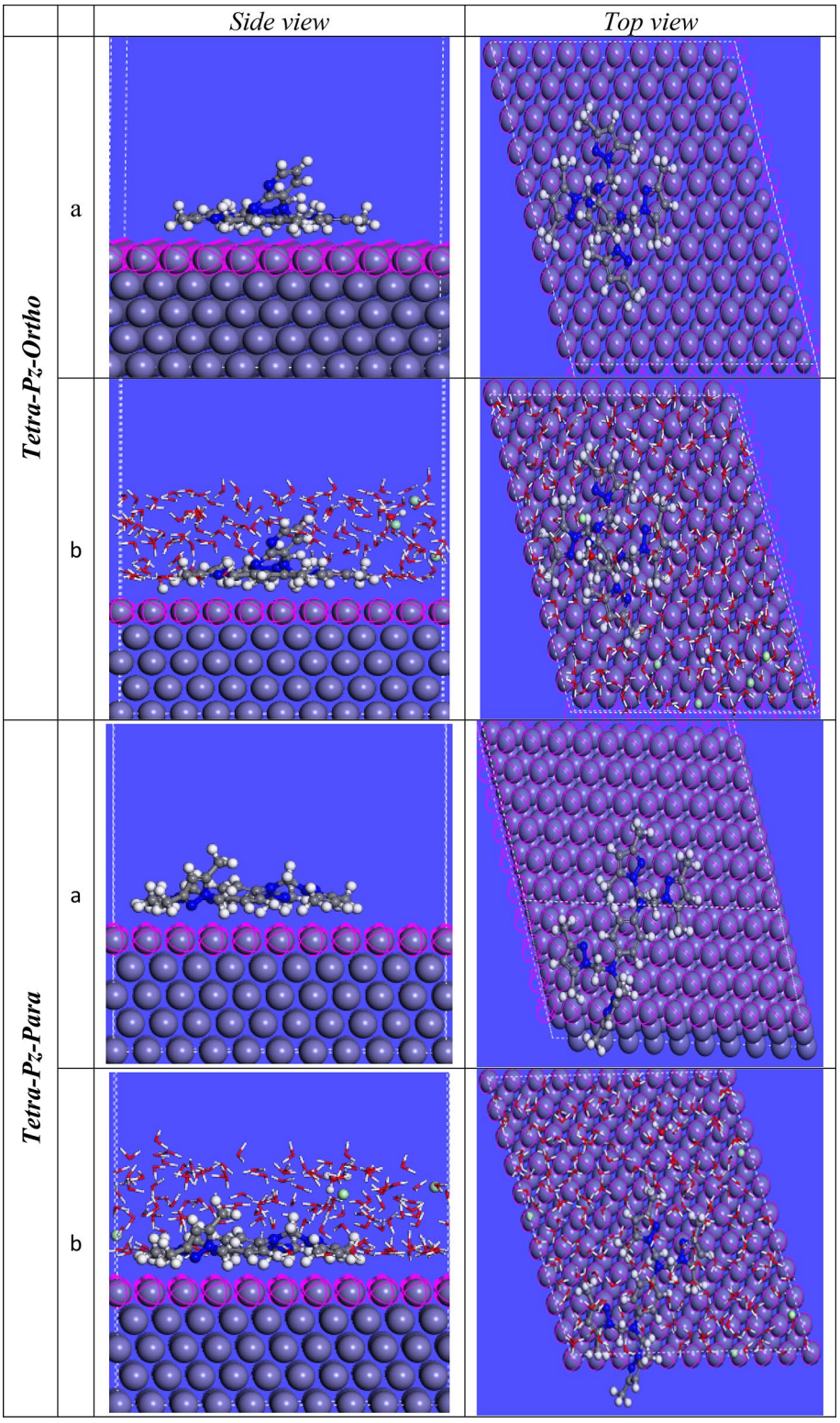

Fig. 17. Side and top views of the most stable low energy configuration for the adsorption of ***Tetra-Pz-Ortho*** and ***Tetra-Pz-Para*** on Fe (110) surface in vacuum (**a**) and aqueous medium (**b**).

System**	Total energy	Adsorption energy	Rigid adsorption energy	Deformation energy	dE_{ad}/dNi	H_3O^+: dE_{ad}/dNi	Cl^-: dE_{ad}/dNi
Fe+(a) gas	-317.89	-291.47	-284.704	-6.766	-291.470	–	–
Fe+ (b) gas	-334.39	-286.27	-288.45	2.176	-286.273	–	–
Fe+(a5H) gas	-412.95	-326.74	-298.55	-28.191	-326.743	–	–
Fe+ (b4H) gas	-414.00	-324.05	-320.01	-4.037	-324.048	–	–
Fe+(a) + 200H_2O + 5HCl	-3556.07	-3636.37	-3699.34	62.967	-10.685	-149.059	-128.593
Fe+ (b) + 200H_2O + 5HCl	-3423.45	-3503.75	-3576.94	73.193	-7.340	-152.975	-142.201
Fe+ (a5H) + 200H_2O + 5HCl	-3429.55	-3509.851	-3579.87	70.020	-7.349	-151.713	-149.699
Fe+ (b4H) + 200H_2O + 5HCl	-3422.931	-3503.23	-3572.92	69.687	-14.819	-152.010	-147.245

Table 9. Outputs and descriptors calculated from Monte Carlo simulations for ***Tetra-Pz-Ortho*** and ***Tetra-Pz-Para*** on Fe (110) (*in gas and solution phases*) (all in kcal/mol). **; (a): ***Tetra-Pz-Ortho ; (b) : Tetra-Pz-Para ; (a5H): Tetra-Pz-Ortho5H*$^+$; ***(b4H): Tetra-Pz-Para4H*$^+$.

	$E_{Interaction}$	$E_{Binding}$
Fe + *Tetra-Pz-Ortho* + 200H_2O + 5HCl	-973.10162	973.10162
Fe + *Tetra-Pz-Para* + 200H_2O + 5HCl	-790.59902	790.59902
Fe + *Tetra-Pz-Ortho5H*$^+$ +200H_2O + 5HCl	-736.46831	736.46831
Fe + *Tetra-Pz-Para4H*$^+$ +200H_2O + 5HCl	-671.66275	671.66275

Table 10. Interaction and binding energies (kcal/mol) obtained from MD simulations for adsorption of the ***Tetra-Pz-Ortho*** and ***Tetra-Pz-Para*** inhibitors (neutral and protonated forms) on Fe (110) surface.

Conclusion

The research work conducted on the application of two newly pyrazole derivatives as corrosion inhibitors for carbon steel in aggressive (HCl) solution can be summarized by the following conclusions:

- Based on the obtained results using the weight loss measurements and electrochemical techniques, the two synthetized molecules ***Tetra-Pz-Ortho*** and ***Tetra-Pz-Para*** acted as effective corrosion inhibitors for C&S in 1 M HCl solution, their inhibition efficiencies increased with increasing concentration inhibitor to reach a maximal inhibition efficacy value of 97.2% and 96.0% at optimum concentration 10^{-3}mol/L. The adsorption model of the two tested molecules followed the Langmuir adsorption isotherm.
- The temperature effect showed that ***Tetra-Pz-Ortho*** has a higher activation energy than ***Tetra-Pz-Para*** and HCl solution. confirming ***Tetra-Pz-Ortho***'s ability to impede the corrosion process. The ΔG^0_{ads} values, calculated of both ***Tetra-Pz-Ortho*** and ***Tetra-Pz-Para***, implying that the two inhibitors were adsorbed on carbon steel surfaces by chemical adsorption.
- Analysis of the EIS diagrams revealed that the corrosion process is mainly controlled by charge transfer, the resistance values R_p increased and the capacity C_{dl} decreased with addition of ***Tetra-Pz-Ortho*** and ***Tetra-Pz-Para*** due to their adsorption onto the metal surface. Potentiodynamic polarization curves revealed that the presence of the two pyrazole derivatives reduced corrosion current density, hence, these tested compounds are mixed type inhibitors.
- The Surface characterization by SEM analysis reflected the deposit of protective film of inhibitors on the carbon steel surface, hence reducing corrosion.
- Elemental analysis results via X-ray Photoelectron Spectroscopy (XPS) revealed that the presence of pyrazolic ring and amine group in these two molecules, with bonds C=C, C−N and C=N, is the most plausible reason to create the chemical interaction between the inhibitors and the metallic surface, indicating that the two tested compounds were chemisorbed on the C&S surface.
- The theoretical approach utilizing density functional theory (DFT) and Monte Carlo/molecular dynamic simulations (MC/MD) simulations for the tested molecules ***Tetra-Pz-Ortho*** and ***Tetra-Pz-Para*** showed good agreement with the experimental results.
- According to MD simulation, the two investigated inhibitors are adsorbed almost parallel to the Fe (110) surface (both in the gas or in the aqueous medium) with a maximum contact.
- The RDF analyzed from the MD results showed that all bond lengths of Fe and atoms (for both ***Tetra-Pz-Ortho*** and ***Tetra-Pz-Para*** atoms) are less than 3.5 Å, as a result, chemical interactions can occur between the atoms of these two molecules and the C&S surface.

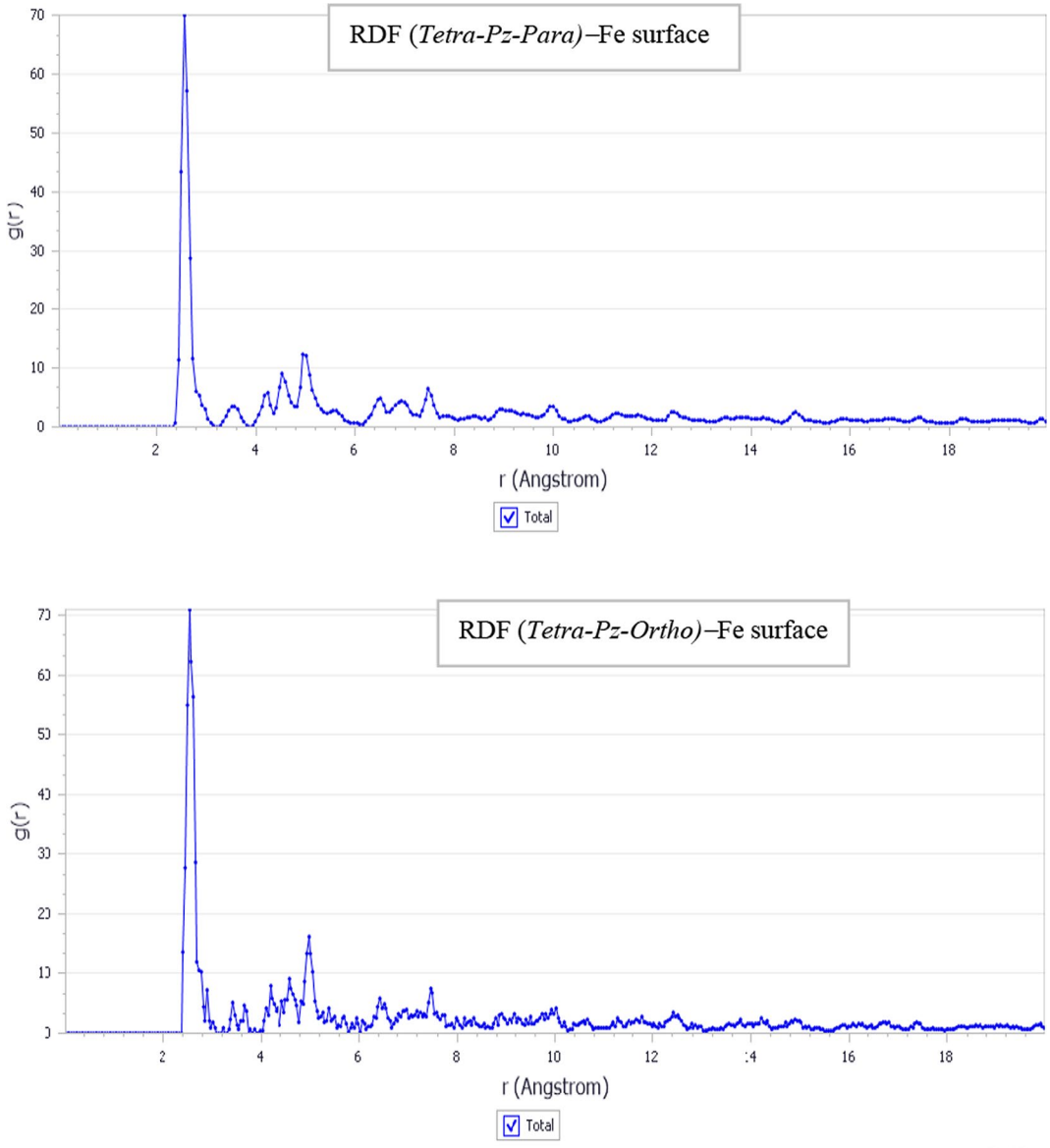

Fig. 18. Radial distribution function of ***Tetra-Pz-Ortho*** and ***Tetra-Pz-Para*** on Fe (110) surface in 1 M HCl solution at 303 K.

Data availability

All data generated or analyzed during this study are included in this published article.

Received: 11 May 2024; Accepted: 20 January 2025
Published online: 29 January 2025

References

1. Fu, F. Fire induced progressive collapse potential assessment of steel framed buildings using machine learning. *J. Constr. Steel Res.* **166**, 105918. https://doi.org/10.1016/j.jcsr.2019.105918 (2020).
2. Rbaa, M. et al. Synthesis of new epoxy glucose derivatives as a non-toxic corrosion inhibitors for carbon steel in molar HCl: experimental, DFT and MD simulation. *Chem. Data Collect.* **27**, 100394. https://doi.org/10.1016/j.cdc.2020.100394 (2020).
3. Belayachi, M. et al. New pyrimidothiazine derivative as Corrosion Inhibitor for Carbon Steel in Acidic Media. *Int. J. Electrochem. Sci.* **10**, 3010–3025. https://doi.org/10.1016/S1452-3981(23)06515-X (2015).
4. Cherrak, K. et al. Two new benzothiazine derivatives as corrosion inhibitors for mild steel in hydrochloric acid medium. *J. Mater. Environ. Sci.* **8**, 636–647 (2017).
5. Jafari, H., Ameri, E., Vakili, M. H. & Berisha, A. Novel Silicon-based schiff-base as corrosion inhibitor for anti-corrosion behavior of API 5L Grade B in 1 M HCl. *Mater. Chem. Phys.* **311**, 128499. https://doi.org/10.1016/j.matchemphys.2023.128499 (2024).
6. Sedik, A. et al. Dardagan Fruit extract as eco-friendly corrosion inhibitor for mild steel in 1 M HCl: Electrochemical and surface morphological studies. *J. Taiwan. Inst. Chem. Eng.* **107**, 189–200. https://doi.org/10.1016/j.jtice.2019.12.006 (2020).

7. Setti, N. et al. Experimental and computational investigation of novel triazole-pyrazole derivative as a synthetic corrosion inhibitor for M-steel in 1.0 M HCl. in *BIO Web of Conferences*. EDP Sciences. 109, 01021. (2024). https://doi.org/10.1051/bioconf/202410901021
8. Arshad, I. et al. Melamine–isatin tris Schiff base as an efficient corrosion inhibitor for mild steel in 0.5 molar hydrochloric acid solution: weight loss, electrochemical and surface studies. *RSC Adv.* **13**, 19301–19311. https://doi.org/10.1039/D3RA00357D (2023).
9. Arshad, I. et al. Melamine-benzaldehyde tris-schiff base as an efficient corrosion inhibitor for mild steel in 0.5 molar hydrochloric acid solution: weight loss, electrochemical, theoretical and surface studies. *Korean J. Chem. Eng.* **40**, 2555–2564. https://doi.org/10.1007/s11814-023-1527-7 (2023).
10. Ahmed, S. K., Ali, W. B. & Khadom, A. A. Synthesis and investigations of heterocyclic compounds as corrosion inhibitors for mild steel in hydrochloric acid. *Int. J. Ind. Chem.* **10**, 159–173. https://doi.org/10.1007/s40090-019-0181-8 (2019).
11. Cherrak, K. et al. Corrosion inhibition of mild steel by new Benzothiazine derivative in a hydrochloric acid solution: experimental evaluation and theoretical calculations. *Chem. Data Collect.* **22**, 100252. https://doi.org/10.1016/j.cdc.2019.100252 (2019).
12. Jafari, H. et al. 4,4'-(((2,2-Dimethylpropane-1,3-Diyl) Bis (Azanediyl)Bis (Methylene) Bis(2-Methoxyphenol) as new reduced form of Schiff Base for protecting API 5L Grade B in 1 M HCl. *Arab. J. Sci. Eng.* **48**, 7359–7372. https://doi.org/10.1007/s13369-022-07281-8 (2023).
13. Jafari, H., Ameri, E., Vakili, M. H. & Berisha, A. Effect of OH position on adsorption behavior of Schiff-base derivatives in corrosion inhibition of carbon steel in 1 M HCl. *Electrochem. Commun.* **159**, 107653. https://doi.org/10.1016/j.elecom.2023.107653 (2024).
14. Jafari, H., Akbarzade, K. & Danaee, I. Corrosion inhibition of carbon steel immersed in a 1 M HCl solution using benzothiazole derivatives. *Arab. J. Chem.* **12**, 1387–1394. https://doi.org/10.1016/j.arabjc.2014.11.018 (2019).
15. Cherrak, K. et al. Electrochemical and theoretical performance of new synthetized pyrazole derivatives as promising corrosion inhibitors for mild steel in acid environment: molecular structure effect on efficiency. *J. Mol. Liq.* **342**, 117507. https://doi.org/10.1016/j.molliq.2021.117507 (2021).
16. Berrissoul, A. et al. Anticorrosion effect of a green sustainable inhibitor on mild steel in hydrochloric acid. *J. Colloid Interf Sci.* **580**, 740–752. https://doi.org/10.1016/j.jcis.2020.07.073 (2020).
17. Belghiti, M. et al. Anti-corrosive properties of 4-amino-3, 5-bis (disubstituted)-1, 2, 4-triazole derivatives on mild steel corrosion in 2 M H3PO4 solution: experimental and theoretical studies. *J. Mol. Liq.* **216**, 874–886. https://doi.org/10.1016/j.molliq.2015.12.093 (2016).
18. Benhiba, F. et al. Combined electronic/atomic level computational, surface (SEM/EDS), chemical and electrochemical studies of the mild steel surface by quinoxalines derivatives anti-corrosion properties in 1 mol· L-1 HCl solution. *J. Chem. Eng.* **28**, 1436–1458. https://doi.org/10.1016/j.cjche.2020.03.002 (2020).
19. ELouadi, Y. et al. Corrosion inhibition of mild steel by new N-heterocyclic compound in 1 M HCl: experimental and computational study. *Der Pharma Chem.* **7**(8), 265–275 (2015).
20. Jafari, H., Ameri, E., Rezaeivala, M., Berisha, A. & Halili, J. Anti-corrosion behavior of two N_2O_4 Schiff-base ligands: experimental and theoretical studies. *J. Phys. Chem. Solids*. **164**, 110645. https://doi.org/10.1016/j.jpcs.2022.110645 (2022).
21. Fadhil, A. A. et al. (S)–6–Phenyl–2, 3, 5, 6–tetrahydroimidazo [2, 1–b] thiazole hydrochloride as corrosion inhibitor of steel in acidic solution: Gravimetrical, electrochemical, surface morphology and theoretical simulation. *J. Mol. Liq.* **276**, 503–518. https://doi.org/10.1016/j.molliq.2018.12.015 (2019).
22. Yilmaz, N., Fitoz, A. & Emregül, K. C. A combined electrochemical and theoretical study into the effect of 2-((thiazole-2-ylimino) methyl) phenol as a corrosion inhibitor for mild steel in a highly acidic environment. *Corros. Sci.* **111**, 110–120. https://doi.org/10.1016/j.corsci.2016.05.002 (2016).
23. Cherrak, K. et al. Performance evaluation of newly synthetized bi-pyrazole derivatives as corrosion inhibitors for mild steel in acid environment. *J. Mol. Struct.* **1261**, 132925. https://doi.org/10.1016/j.molstruc.2022.132925 (2022).
24. Chafiq, M., Chaouiki, A., Al-Hadeethi, M. R., Salghi, R. & Chung, I. M. A joint experimental and theoretical investigation of the corrosion inhibition behavior and mechanism of hydrazone derivatives for mild steel in HCl solution. *Colloids Surf.* **610**, 125744. https://doi.org/10.1016/j.colsurfa.2020.125744 (2021).
25. Solmaz, R., Altunbaş, E. & Kardaş, G. Adsorption and corrosion inhibition effect of 2-((5-mercapto-1, 3, 4-thiadiazol-2-ylimino) methyl) phenol Schiff base on mild steel. *Mater. Chem. Phys.* **125**, 796–801. https://doi.org/10.1016/j.matchemphys.2010.09.056 (2011).
26. Elshaier, Y. A., Barakat, A., Al-Qahtany, B. M., Al-Majid, A. M. & Al-Agamy, M. H. Synthesis of pyrazole-thiobarbituric acid derivatives: antimicrobial activity and docking studies. *Molecules* **21**, 1337. https://doi.org/10.3390/molecules21101337 (2016).
27. Shah, J. J., Khedkar, V., Coutinho, E. C. & Mohanraj, K. Design, synthesis and evaluation of benzotriazole derivatives as novel antifungal agents. Bioorg. *Med. Chem. Lett.* **25**, 3730–3737. https://doi.org/10.1016/j.bmcl.2015.06.025 (2015).
28. Kaddouri, Y. et al. Synthesis, characterization, reaction mechanism prediction and biological study of mono, bis and tetrakis pyrazole derivatives against Fusarium oxysporum f. sp. Albedinis with conceptual DFT and ligand-protein docking studies. *Bioorg. Chem.* **110**, 104696. https://doi.org/10.1016/j.bioorg.2021.104696 (2021).
29. Kaddouri, Y. et al. ADME-Tox predictions, and antimicrobial evaluation of novel mono-and tetra-alkylated pyrazole and triazole ligands. *J. Chem.* **2021**, 6663245. https://doi.org/10.1155/2021/6663245 (2021).
30. Daoudi, M. et al. Synthesis of N,N′-bis and N,N,N′,N′-tetra-[(3, 5-di-substituted-1-pyrazolyl) methyl] para-phenylenediamines: new candidate ligands for metal complex wires. *Tetrahedron* **62**, 3123–3127. https://doi.org/10.1016/j.tet.2006.01.034 (2006).
31. Daoudi, M. et al. Crystal structure of N, N, N', N'-tetra-[(3, 5-dimethyl-1-pyrazolyl) methyl]-para-phenylenediamine. *Molecules* **8**, 269–274. https://doi.org/10.3390/80200269 (2003).
32. A.S.f. Testing, Materials, ASTM G1-03: standard practice for preparing, cleaning, and evaluating corrosion test specimens, ASTM, (2004).
33. Frisch, M. gaussian 09, Revision d. 01, Gaussian. 201 (2009).
34. Cherrak, K. et al. Pyrazole carbohydrazide as corrosion inhibitor for mild steel in HCl medium: experimental and theoretical investigations. *Surf. Interfaces*. **20**, 100578. https://doi.org/10.1016/j.surfin.2020.100578 (2020).
35. BIOVIA, D. S. BIOVIA materials studio. 92121 (2016).
36. Sun, H. COMPASS: an ab initio force-field optimized for condensed-phase applications overview with details on alkane and benzene compounds. *J. Phys. Chem.* **102**, 7338–7364. https://doi.org/10.1021/jp980939v (1998).
37. Belghiti, M. et al. Computational simulation and statistical analysis on the relationship between corrosion inhibition efficiency and molecular structure of some hydrazine derivatives in phosphoric acid on mild steel surface. *Appl. Surf. Sci.* **491**, 707–722. https://doi.org/10.1016/j.apsusc.2019.04.125 (2019).
38. Tourabi, M., Nohair, K., Traisnel, M., Jama, C. & Bentiss, F. Electrochemical and XPS studies of the corrosion inhibition of carbon steel in hydrochloric acid pickling solutions by 3, 5-bis (2-thienylmethyl)-4-amino-1, 2, 4-triazole. *Corros. Sci.* **75**, 123–133. https://doi.org/10.1016/j.corsci.2013.05.023 (2013).
39. Berrissoul, A. et al. Exploitation of a new green inhibitor against mild steel corrosion in HCl: experimental, DFT and MD simulation approach. *J. Mol. Liq.* **349**, 118102. https://doi.org/10.1016/j.molliq.2021.118102 (2022).
40. Gong, W., Yin, X., Liu, Y., Chen, Y. & Yang, W. 2-Amino-4-(4-methoxyphenyl)-thiazole as a novel corrosion inhibitor for mild steel in acidic medium. *Prog Org. Coat.* **126**, 150–161. https://doi.org/10.1016/j.porgcoat.2018.10.001 (2019).

41. Attou, A. et al. Experimental studies and computational exploration on the 2-amino-5-(2-methoxyphenyl)-1, 3, 4-thiadiazole as novel corrosion inhibitor for mild steel in acidic environment. *Colloids Surf.* **604**, 125320. https://doi.org/10.1016/j.colsurfa.2020.125320 (2020).
42. Popova, A., Christov, M. & Vasilev, A. Mono-and dicationic benzothiazolic quaternary ammonium bromides as mild steel corrosion inhibitors. Part II: Electrochemical impedance and polarisation resistance results. *Corros. Sci.* **53**, 1770–1777. https://doi.org/10.1016/j.corsci.2011.01.055 (2011).
43. Verma, C., Ebenso, E. E. & Quraishi, M. Molecular structural aspects of organic corrosion inhibitors: influence of–CN and–NO2 substituents on designing of potential corrosion inhibitors for aqueous media. *J. Mol. Liq.* **316**, 113874. https://doi.org/10.1016/j.molliq.2020.113874 (2020).
44. Growcock, F. & Jasinski, R. Time-resolved impedance spectroscopy of mild steel in concentrated hydrochloric acid. *J. Electrochem. Soc.* **136**, 2310. https://doi.org/10.1149/1.2097847 (1989).
45. Kharbach, Y. et al. Anticorrosion performance of three newly synthesized isatin derivatives on carbon steel in hydrochloric acid pickling environment: electrochemical, surface and theoretical studies. *J. Mol. Liq.* **246**, 302–316. https://doi.org/10.1016/j.molliq.2017.09.057 (2017).
46. Berrissoul, A. et al. Assessment of corrosion inhibition performance of origanum compactum extract for mild steel in 1 M HCl: weight loss, electrochemical, SEM/EDX, XPS, DFT and molecular dynamic simulation. *Ind. Crops Prod.* **187**, 115310. https://doi.org/10.1016/j.indcrop.2022.115310 (2022).
47. Bouanis, M. et al. Corrosion inhibition performance of 2, 5-bis (4-dimethylaminophenyl)-1, 3, 4-oxadiazole for carbon steel in HCl solution: Gravimetric, electrochemical and XPS studies. *Appl. Surf. Sci.* **389**, 952–966. https://doi.org/10.1016/j.apsusc.2016.07.115 (2016).
48. Wang, Q. et al. Insight into the anti–corrosion performance of Artemisia argyi leaves extract as eco–friendly corrosion inhibitor for carbon steel in HCl medium. *Sustainable Chem. Pharm.* **27**, 100710. https://doi.org/10.1016/j.scp.2022.100710 (2022).
49. Tawfik, S. M. & Negm, N. A. Vanillin-derived non-ionic surfactants as green corrosion inhibitors for carbon steel in acidic environments. *Res. Chem. Intermed.* **42**, 3579–3607. https://doi.org/10.1007/s11164-015-2233-9 (2016).
50. Zarrok, H. et al. Gravimetric and Electrochemical evaluation of 1-allyl-1Hindole-2,3-dione of Carbon Steel Corrosion in Hydrochloric Acid. *Int. J. Electrochem. Sci.* **7**, 10338–10357. https://doi.org/10.1016/S1452-3981(23)16281-X (2012).
51. Biswas, A., Mourya, P., Mondal, D., Pal, S. & Udayabhanu, G. Grafting effect of gum acacia on mild steel corrosion in acidic medium: Gravimetric and electrochemical study. *J. Mol. Liq.* **251**, 470–479. https://doi.org/10.1016/j.molliq.2017.12.087 (2018).
52. Yıldız, R. An electrochemical and theoretical evaluation of 4, 6-diamino-2-pyrimidinethiol as a corrosion inhibitor for mild steel in HCl solutions. *Corros. Sci.* **90**, 544–553. https://doi.org/10.1016/j.corsci.2014.10.047 (2015).
53. Verma, C., Ebenso, E., Bahadur, I., Obot, I. & Quraishi, M. 5-(Phenylthio)-3H-pyrrole-4-carbonitriles as effective corrosion inhibitors for mild steel in 1 M HCl: experimental and theoretical investigation. *J. Mol. Liq.* **212**, 209–218. https://doi.org/10.1016/j.molliq.2015.09.009 (2015).
54. Hassouni, H. E. et al. Corrosion inhibition, surface adsorption and computational studies of new sustainable and green inhibitor for mild steel in acidic medium. *Inorg. Chem.* **143**, 109801. https://doi.org/10.1016/j.inoche.2022.109801 (2022).
55. Mohanty, A., Kumar, S. & Tiwari, S. Assessment of N-(4H-1, 2, 4-triazol-4-yl) octanamide as hydrochloric acid corrosion inhibitor for mild steel. *Mater. Today Commun.* **27**, 102439. https://doi.org/10.1016/j.mtcomm.2021.102439 (2021).
56. Yaro, A. S., Khadom, A. A. & Wael, R. K. Apricot juice as green corrosion inhibitor of mild steel in phosphoric acid. *Alexandria Eng. J.* **52**, 129–135. https://doi.org/10.1016/j.aej.2012.11.001 (2013).
57. Tayebi, H. et al. An electrochemical and theoretical evaluation of new quinoline derivative as a corrosion inhibitor for carbon steel in HCl solutions. *Der Pharmacia Lett.* **6**(6), 20–34 (2014).
58. Oubaaqa, M. et al. Insight into the corrosion inhibition of new amino-acids as efficient inhibitors for mild steel in HCl solution: experimental studies and theoretical calculations. *J. Mol. Liq.* **334**, 116520. https://doi.org/10.1016/j.molliq.2021.116520 (2021).
59. Singh, A. et al. Solvent-free microwave assisted synthesis and corrosion inhibition study of a series of hydrazones derived from thiophene derivatives: experimental, surface and theoretical study. *J. Mol. Liq.* **283**, 788–803. https://doi.org/10.1016/j.molliq.2019.03.126 (2019).
60. Singh, A. K. & Quraishi, M. Effect of 2, 2′ benzothiazolyl disulfide on the corrosion of mild steel in acid media. *Corros. Sci.* **51**, 2752–2760. https://doi.org/10.1016/j.corsci.2009.07.011 (2009).
61. Mostafa, M. A., Bowley, R. M., Racys, D. T., Henry, M. C. & Sutherland, A. Iron (III)-catalyzed chlorination of activated arenes. *J. Inorg. Chem.* **82**, 7529–7537. https://doi.org/10.1021/acs.joc.7b01225 (2017).
62. Berrissoul, A. et al. Evaluation of Lavandula Mairei extract as green inhibitor for mild steel corrosion in 1 M HCl solution. Experimental and theoretical approach. *J. Mol. Liq.* **313**, 113493. https://doi.org/10.1016/j.molliq.2020.113493 (2020).
63. Zaidon, F. H., Kassim, K., Zaki, H. M., Embong, Z. & Hashim, N. Z. N. Adsorption and corrosion inhibition accomplishment for thiosemicarbazone derivatives for mild steel in 1.0 M HCl medium: electrochemical, XPS and DFT studies. *J. Mol. Liq.* **329**, 115553. https://doi.org/10.1016/j.molliq.2021.115553 (2021).
64. Hashim, N. Z. N., Kassim, K., Zaki, H. M., Alharthi, A. I. & Embong, Z. XPS and DFT investigations of corrosion inhibition of substituted benzylidene Schiff bases on mild steel in hydrochloric acid. *Appl. Surf. Sci.* **476**, 861–877. https://doi.org/10.1016/j.apsusc.2019.01.149 (2019).
65. Zarrok, H. et al. Corrosion control of carbon steel in phosphoric acid by purpald–weight loss, electrochemical and XPS studies. *Corros. Sci.* **64**, 243–252. https://doi.org/10.1016/j.corsci.2012.07.018 (2012).
66. Bentiss, F. et al. Corrosion control of mild steel using 3, 5-bis (4-methoxyphenyl)-4-amino-1, 2, 4-triazole in normal hydrochloric acid medium. *Corros. Sci.* **51**, 1628–1635. https://doi.org/10.1016/j.corsci.2009.04.009 (2009).
67. Abouchane, M. et al. Insight into the corrosion inhibition performance of two quinoline-3-carboxylate derivatives as highly efficient inhibitors for mild steel in acidic medium: experimental and theoretical evaluations. *J. Mol. Liq.* **360**, 119470. https://doi.org/10.1016/j.molliq.2022.119470 (2022).
68. Rbaa, M. et al. Green synthesis of novel carbohydrate polymer chitosan oligosaccharide grafted on d-glucose derivative as bio-based corrosion inhibitor. *J. Mol. Liq.* **322**, 114549. https://doi.org/10.1016/j.molliq.2020.114549 (2021).
69. Singh, A., Ansari, K. & Quraishi, M. Chondroitin sulfate as a green corrosion inhibitor for zinc in 26% ammonium chloride solution: Electrochemical and surface morphological analysis. *Colloids Surf.* **607**, 125465. https://doi.org/10.1016/j.colsurfa.2020.125465 (2020).
70. Gabler, C. et al. Corrosion properties of ammonium based ionic liquids evaluated by SEM-EDX, XPS and ICP-OES. *Green. Chem.* **13**, 2869–2877. https://doi.org/10.1039/C1GC15148G (2011).
71. Saranya, J. et al. Experimental and computational approaches on the pyran derivatives for acid corrosion. *Colloids Surf.* **603**, 125231. https://doi.org/10.1016/j.colsurfa.2020.125231 (2020).
72. MarvinSketch & Software Version: 18.22, ChemAxon Ltd. (2018).
73. Rbaa, M. et al. Synthesis, bioinformatics and biological evaluation of novel pyridine based on 8-hydroxyquinoline derivatives as antibacterial agents: DFT, molecular docking and ADME/T studies. *J. Mol. Struct.* **1244**, 130934. https://doi.org/10.1016/j.molstruc.2021.130934 (2021).
74. Belghiti, M. E. et al. Inhibition effect of E and Z conformations of 2-pyridinealdazine on mild steel corrosion in phosphoric acid. *Anti-Corros Methods Mater.* **64**, 23–35. https://doi.org/10.1108/acmm-11-2015-1594 (2017).
75. Yarnell, J. L., Katz, M., Wenzel, R. G. & Koenig, S. Structure factor and radial distribution function for liquid argon at 85 K. *Phys. Rev.* **7**, 2130. https://doi.org/10.1103/physreva.7.2130 (1973).

76. Daoud, D., Douadi, T., Hamani, H., Chafaa, S. & Al-Noaimi, M. Corrosion inhibition of mild steel by two new S-heterocyclic compounds in 1 M HCl: experimental and computational study. *Corros. Sci.* **94**, 21–37. https://doi.org/10.1016/j.corsci.2015.01.025 (2015).

Acknowledgements
The authors extend their appreciation to the Researchers Supporting Project, King Saud University, Riyadh, Saudi Arabia for funding this work through grant number RSPD2024R566.

Author contributions
Nawal Setti & Asma Barrahi & Yassine Kaddouri: Formal analysis; Investigation; Methodology; Writing - original draft.Halima Outada & Ali Dafali: Conceptualization; Data curation; Formal analysis; Methodology; Project administration; Resources; Supervision, Validation; Visualization; Writing - original draft; Writing - review & editing.Mohamed Maatallah & Taibi Ben Hadda & Abhinay Thakur & Rachid Touzani & Khalid Karrouchi & Hatem A. Abuelizz & Burak Dikici & Abdelkader Zarrouk: Software; Writing - original draft; Writing - review & editing.

Funding
There were no research Grants for this work from any funding agencies.

Declarations

Competing interests
The authors declare no competing interests.

Ethical approval
Not applicable.

Consent to participate
Not applicable.

Consent for publication
Not applicable.

Additional information
Correspondence and requests for materials should be addressed to A.Z. or A.D.

Reprints and permissions information is available at www.nature.com/reprints.

Publisher's note Springer Nature remains neutral with regard to jurisdictional claims in published maps and institutional affiliations.